Available online at www.sciencedirect.com

ScienceDirect

Geochimica et Cosmochimica Acta 328 (2022) 19–36

Geochimica et Cosmochimica Acta

www.elsevier.com/locate/gca

Oxidizing fluids associated with detachment hosted hydrothermal systems: Example from the Suye hydrothermal field on the ultraslow-spreading Southwest Indian Ridge

Shili Liao [a], Chunhui Tao [a,*], John W. Jamieson [b], Jia Liu [c], Chuanwei Zhu [d], Fernando J.A.S. Barriga [e], Wei Li [a], Jin Liang [a], Weifang Yang [a], Jianping Zhou [a], Xianming Deng [a], Junyu Yu [a]

[a] *Key Laboratory of Submarine Geosciences, Second Institute of Oceanography, Ministry of Natural Resources, Hangzhou 310012, Zhejiang, China*

[b] *Department of Earth Sciences, Memorial University of Newfoundland, St. John's, NL A1B 3X5, Canada*

[c] *School of Earth Sciences, Zhejiang University, Hangzhou 310001, Zhejiang, China*

[d] *Institute of Geochemistry, Chinese Academy of Sciences, Guiyang 550081, China*

[e] *Dom Luiz Institute and Department of Geology, University of Lisbon, 1749-016 Lisbon, Portugal*

Received 19 October 2021; accepted in revised form 23 April 2022; available online 30 April 2022

Abstract

The redox state of hydrothermal fluids on mid-ocean ridges, which is indirectly affected by the depth of hydrothermal circulation and crustal permeability, plays an important role on the diversity of hydrothermal precipitates and associated ecosystems. Primary hydrothermal fluids that circulate along detachment faults are generally reducing as a result of the serpentinization of ultramafic rocks, while significant seawater infiltration may shift the redox state from reducing to oxidizing. However, the depth of penetration of oxidizing fluids into detachment related systems remain unclear, largely because current observations are based primarily on hydrothermal products that precipitated at the seafloor. Here, we report the first observations of oxidizing mineral assemblages in stockwork samples from the Suye hydrothermal field on the ultraslow spreading Southwest Indian Ridge. This field is hosted by mafic lithologies, while the low As, high Ni and Co contents, and high Au/As, Ag/As, and Ni/As ratios in pyrite from the stockwork samples indicate that the fluids reacted with both mafic and ultramafic rocks in the subseafloor. The high $\delta^{34}S$ values (average of 9.8‰) indicate a high proportion (up to 50%) of seawater derived reduced sulfur involved in the stockwork zone formation. The high homogenization temperatures (~320 °C) and salinity (~12 wt.% NaCl) of fluid inclusions indicate that the stockwork zone of Suye was formed by a fluid that underwent phase separation deeper in the system that was subsequently diluted by 4–5 times subsurface seawater. The deep penetration of seawater is facilitated by the unique tectonic setting of the Suye hydrothermal field, which occurs between the two stage detachment faults that creates high permeability. Our findings demonstrate that hydrothermal fluid associated with detachment faults could be oxidized below the subsurface stockwork zone, and that deep-rooted detachment faults at ultraslow-spreading ridges can sustain both reducing and oxidizing hydrothermal systems in the same fault system. These results call for a reevaluation of the fate of base metal in ultramafic hosted hydrothermal fields.

Keywords: Stockwork mineralization; Oxidizing fluid; S isotope; Suye hydrothermal field; Southwest Indian Ridge

* Corresponding author.
E-mail addresses: taochunhuimail@163.com, taochunhui@sio.org.cn (C. Tao).

https://doi.org/10.1016/j.gca.2022.04.025
0016-7037/

1. INTRODUCTION

Hydrothermal activity on mid ocean ridge (MOR) systems is an important process for heat and chemical exchange between the ocean and crust, creating important habitat for biological communities on the ocean floor (Elderfield and Schultz, 1996), and formation of metal-rich massive sulfide ore deposits (Hannington et al., 2011). The redox state of hydrothermal fluids is a key chemical control on the concentration of elements in hydrothermal fluids and their precipitates (Seyfried and Ding, 1995; Kawasumi and Chiba, 2017), and will influence the composition of associated mineral deposits and the composition and diversity of vent-associated biological populations (Sarrazin et al., 1999; Mcdermott et al., 2020).

At MOR systems, the redox state of hydrothermal fluid is indirectly affected by the depth of hydrothermal circulation, which controls the layers of oceanic crust and mantle that the fluid will react with, and permeability, which controls the influx of seawater into the system. Due to limited magma supply along ultraslow-spreading ridges (<4 mm/yr; Dick et al., 2003), tectonic mediated seafloor spreading often results in large scale, steeply dipping, detachment faults that facilitate seawater circulation to the deep oceanic lithosphere (Cannat et al., 2019). Recent seismic observations from slow and ultraslow spreading ridges indicate that deep hydrothermal alteration can result in extensive serpentinization of the lithospheric mantle (Schlindwein and Schmid, 2016), which would result in highly reducing hydrothermal fluids due primarily to the addition of H_2 (Charlou et al., 2002; Mccollom and Bach, 2009; Connelly et al., 2012; Verlaguet et al., 2021). By contrast, oxidizing systems, or less reducing systems that typically precipitate iron-oxides, are expected due to shallow seawater infiltration (Fouquet et al., 2010; Dekov et al., 2018 and references therein). However, present observations of oxidizing hydrothermal systems are based exclusively on surface hydrothermal products. The depth of penetration of oxidizing fluids, and when and where the hydrothermal fluid become oxidizing are still poorly constrained. Furthermore, oxidizing hydrothermal systems have never been documented among the currently confirmed hydrothermal fields on ultraslow-spreading ridges (InterRidge Vents Database Ver. 3.4).

In this study, we report the first documentation of a hydrothermal system (Suye hydrothermal field, Southwest Indian Ridge (SWIR); Fig. 1) associated with a detachment fault on the ultraslow spreading ridge that features an oxidized mineral assemblage. This field is hosted by mafic lithologies. We report high hematite and magnetite contents intergrown with pyrite in exposed stockwork-type samples associated with the subsurface stringer zone of the hydrothermal system (Hannington et al., 1998). This oxide-rich mineralogy is significantly different from typical sulfide-rich mineralogy documented at hydrothermal fields on ultraslow-spreading ridges (Tao et al., 2014; Webber et al., 2015; Yang et al., 2016; Liao et al., 2018; Snook et al., 2018). We combine results from studies of the mineralogy, and geochemical and sulfur isotopic compositions of pyrite to present evidence that the stockwork zone of the Suye hydrothermal field was formed under oxidizing and high seawater flux conditions. This finding gives new insights to hydrothermal activities on detachment faults, and it implies higher seawater rock interaction on multi-stage detachment faults.

2. GEOLOGICAL BACKGROUND AND SAMPLES

The Suye hydrothermal field (49.73 °E, 37.78 °S, originally named Longqi-3) is located on the southern rift valley wall of the 28th segment on the ultraslow-spreading SWIR (Fig. 1a), approximately 5 km south of the ridge axis, at a water depth of approximately 2200–2400 m. This area is part of the Dragon Horn oceanic core complex, which is composed of a twin detachment fault system (Fig. 1b and 1c; Yu et al., 2018; Tao et al., 2020). The older, first stage detachment fault (DF1) forms a dome-shaped surface, and is steeply dipping (~65°) into the mantle to a depth of more than 13 km (Yu et al., 2018). The younger, active secondary detachment fault (DF2) occurs at the basaltic scarp of DF1 (Tao et al., 2020). The inactive Suye field and active Longqi-1 hydrothermal field that occurs ~7.5 km to the west of Suye, are located on the footwall and hanging wall of DF2, respectively (Fig. 1b). Two additional plume anomalies were detected on the lateral boundaries of DF1, suggesting the presence of additional hydrothermal activity (Tao et al., 2014).

Deep-tow observations and grab sampling revealed that the mineralization at Suye is hosted by intensely chloritized basalt and basaltic breccia, and distributed along a NE-striking normal fault on the secondary detachment surface (DF2, Fig. 1d), covering an area approximately 300 × 250 m. Ultramafic rocks that exhibit differing degrees of serpentinization were collected on or near the detachment surface of DF2 (Tao et al., 2020; Wu et al., 2021; Fig. 1b). No evidence of fluid venting, such as smoke, shimmering water, bacterial mats, or vent fauna, has been observed, suggesting that this field is inactive or even extinct (Jamieson and Gartman, 2020). Three stations of mineralized samples were collected by TV-grab during the 34th and 40th cruises in 2015–2016 by RVs Dayangyihao and Xiangyanghong 10, respectively. Based on mineral intergrowth and replacement textures, the samples are divided into stockwork and semi-massive type mineralization. The stockwork samples are characterized by a chloritized basalt breccia wall rock cut by veins and veinlets composed by sulfide and iron oxide minerals (Fig. 2a–c). These samples represent the feeder zone through which hydrothermal fluids rise towards the seafloor. Pyrite-hematite-quartz veins, and chalcopyrite-pyrite-magnetite-hematite-quartz veins are visible in hand specimens (Fig. 2). Petrographic observations indicate that the main hydrothermal minerals (which represent 20–30% of the total sample volume) of the stockwork samples are pyrite, chalcopyrite, magnetite, hematite, and ilmenite (Fig. 3). The semi-massive sulfide samples contain 25–50 vol% of massive sulfides, and are mainly composed of pyrite, pyrrhotite, chalcopyrite, and minor sphalerite (Fig. 2d). The

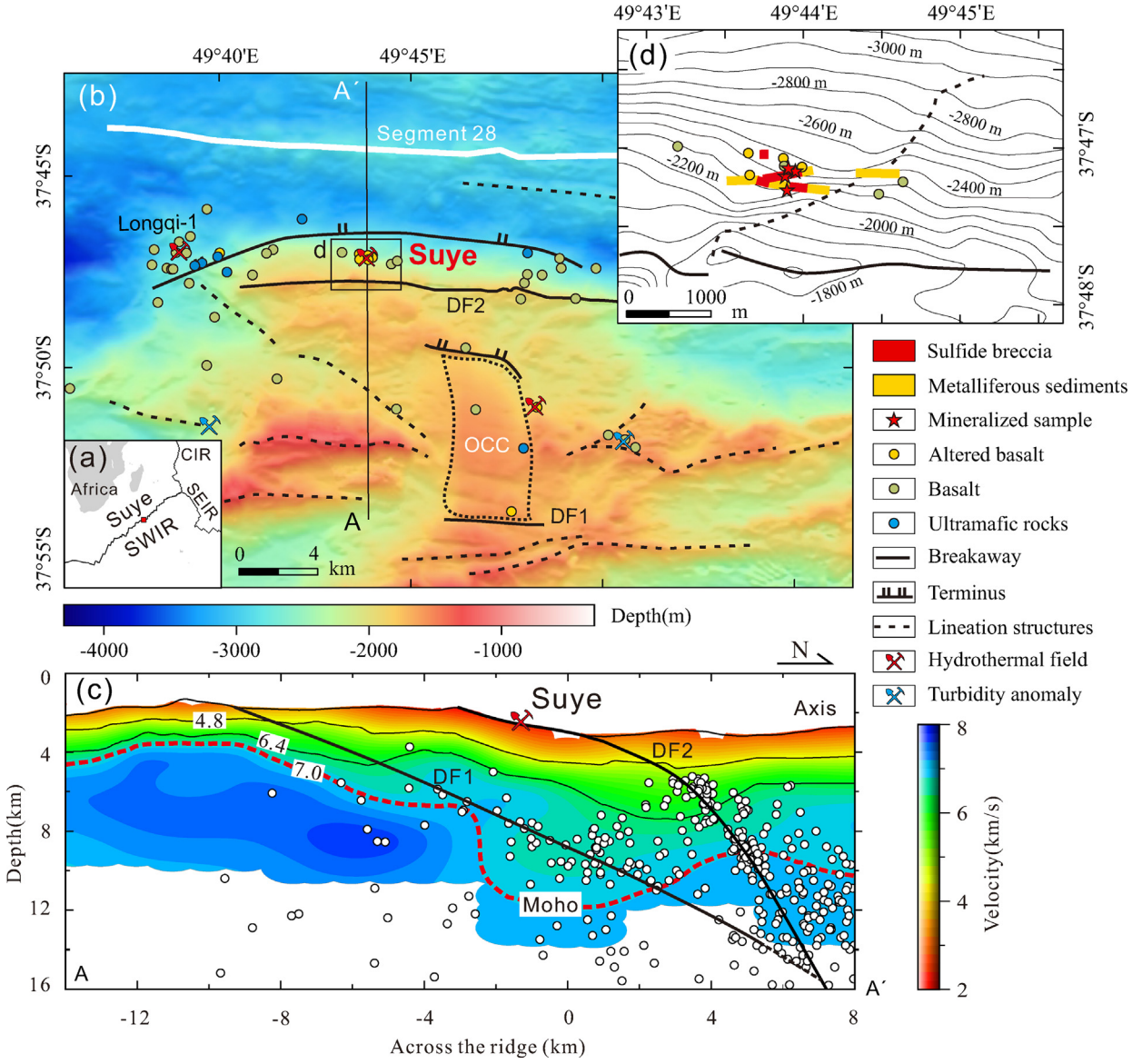

Fig. 1. (a) Location and (b) setting of the Suye hydrothermal field. Ridge axis was inferred based on the direction of gravity anomalies. The detachment fault and lineation structures are those of Tao et al. (2020); the lithology of the sampling stations was from Tao et al. (2020), Wu et al. (2021) and this study. (c) Inferred location of detachment faults based on distribution of seismic epicenters. The micro-earthquake and seismic velocity profile are from Tao, et al. (2020) and Zhao, et al. (2013), respectively. The depth of the Moho was defined by velocity 7.0 km/s. (d) Distribution of hydrothermal mineralization at Suye was mapped by deep-tow observations and sampling. The stars and circles represent locations of samples collected by TV-grab. Topography data for b and d are from multibeam bathymetric surveys.

matrix is mainly composed of quartz with minor basaltic and early stage mineralized debris. Four typical samples were chosen for analysis in this study.

(a) TVG05-1: stockwork sulfide rich sample

This sample is dark gray in color, and contains abundant disseminated mineralization. The matrix consists of intensively altered basalt that comprises chlorite, quartz, epidote, and sphene. The matrix is generally fractured and cross cut by pyrite-hematite-quartz veins or hematite-pyrite-quartz veins (Fig. 2a).

(b) TVG21-2: stockwork sulfide rich sample

This sample is reddish-brown in color and consists primarily of chloritized basaltic breccia (Fig. 2b). The brecciated clasts are irregular shaped, with a maximum diameter of 4–5 cm. Abundant disseminated euhedral to subhedral cubic limonite crystals was identified, representing the weathered product of pyrite. Two types of sulfide mineralization were observed in the fractured breccia groundmass. Pyrite-chalcopyrite-hematite-magnetite rich quartz cements the basaltic breccia and is cut cross and replaced by pyrite bearing quartz veins (Fig. 2b).

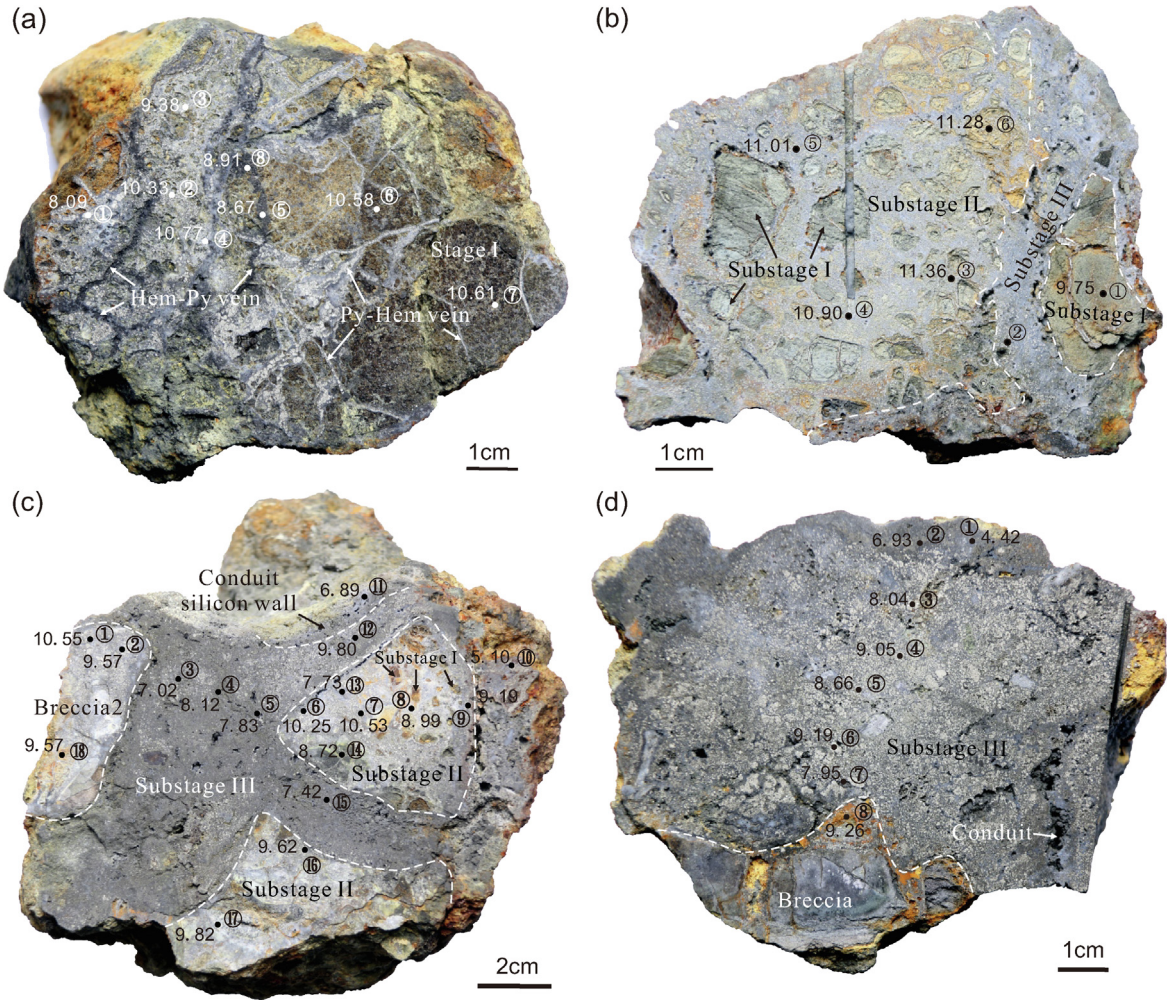

Fig. 2. Hand specimen of the samples collected from Suye. Black and white dots represent the micro drilling samples for sulfur isotope analysis. Numbers in circles represented sample numbers, and the results ($\delta^{34}S$ values in permil) are list besides the sampling position. (a) Stockwork sample: disseminated pyrite mineralized basalt (substage I) was cut by pyrite-hematite, and hematite-pyrite bearing quartz veins (substage I/II), TVG05; (b) Stockwork sample: disseminated pyrite mineralization (substage I) in basalt was cemented by pyrite-chalcopyrite-magnetite-hematite-bearing quartz (substage II), and then cut by pyrite bearing quartz veins (substage III); the pyrite in the breccia was partially limonitized, TVG21-2; (c) Stockwork sample: two stages of breccia were observed, and the first-stage breccia exhibited disseminated pyrite mineralization features (substage I) and was cemented by pyrite-chalcopyrite-magnetite-hematite-bearing quartz (substage II), which was subsequently cemented by pyrite-quartz veins as breccia (substage III), TVG21-6; (d) Semi-massive sample: pyrite-bearing quartz and weakly altered basalt breccia were observed, TVG21-3.

(c) TVG21-6: stockwork sulfide rich sample

This sample consists of a cemented sulfide breccia (Fig. 2c). There are two types of breccia: an early highly mineralized basaltic breccia (comparable with sample TVG05-1), with irregularly-shaped clasts of generally less than 0.5 cm. This texture is cemented by pyrite-hematite-chalcopyrite bearing quartz. This early texture is over-printed by a late-stage pyrite bearing quartz.

(d) TVG21-3: semi-massive sulfide rich sample

This silica-rich sample contains semi-massive (25–30% by volume) pyrite with minor chalcopyrite and pyrrhotite, with a siliceous conduit wall on the edge of the sample (Fig. 2d). A small amount of weakly altered basalt breccia with small diameters were cemented.

3. METHODS

3.1. Micro-drilling

Micro-drilling was carried out using a MICRODRILL SYSTEM at the State Key Laboratory of Ore Deposit Geochemistry in the Institute of Geochemistry at the Chinese Academy of Sciences in Guiyang. This instrument can conduct in situ sampling during optical observations to ensure the purity of each collected sample. The diameter of the

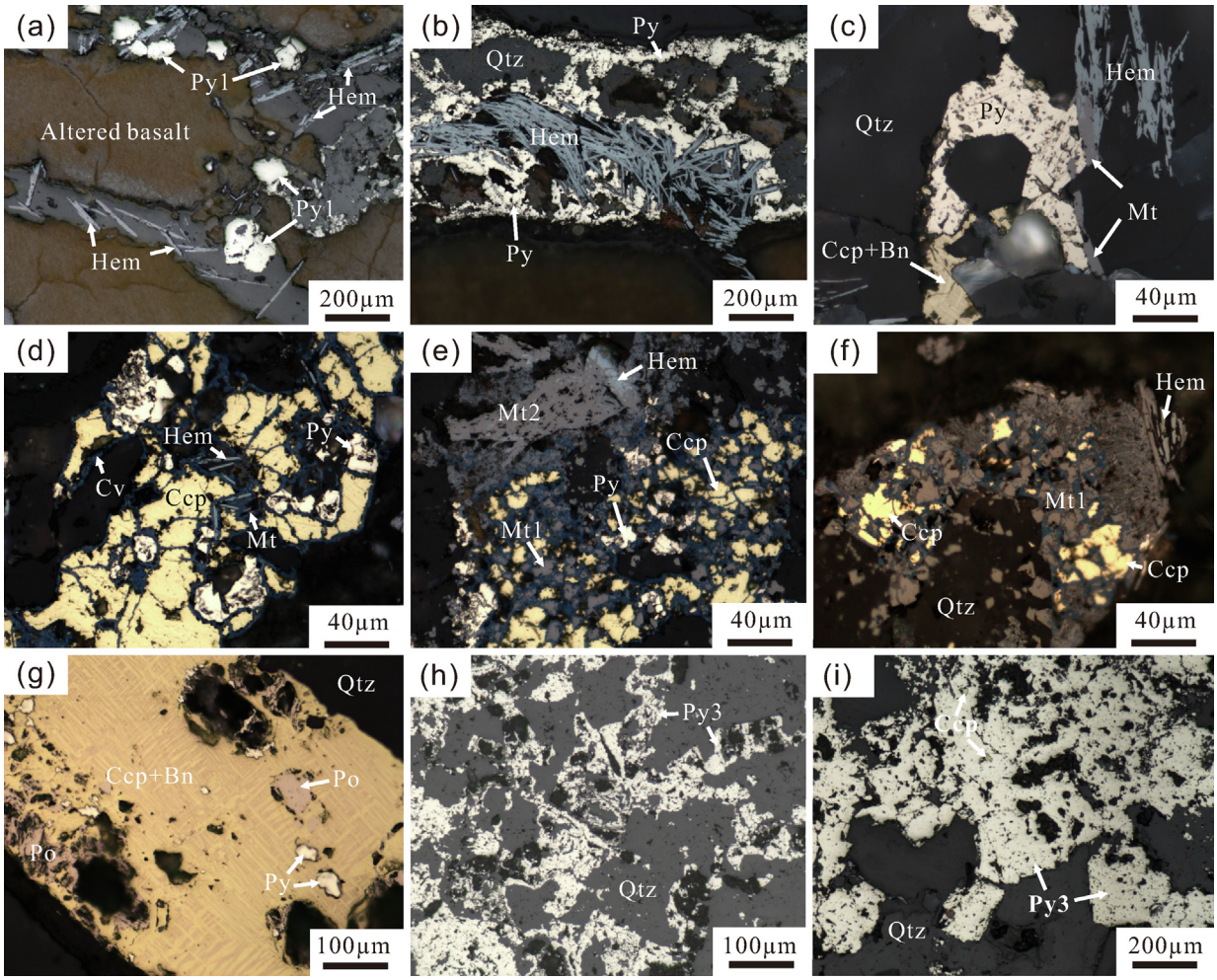

Fig. 3. Microphotographs of the samples collected from Suye. (a) Py1 coexisted with Hem in the first-stage breccia; (b) Py overgrowth with Hem; (c) Ccp and Bn overgrowth with Py in quartz vein, Py intergrowth with Mt and Hem, which partially turned into Mt; (d) Ccp intergrowth with Hem and Mt replacing Py in quartz vein; (e) Mt1 intergrowth with Ccp replacing Py in quartz vein and subsequent replacement by Hem, which has partially been replaced by Mt2; (f) Mt intergrowth with Ccp and subsequently replaced by Hem;(g)Py3 replaced by Po and Ccp + Bn in the semi-massive sample; (h) and (i) Py3 with minor chalcopyrite in the quartz; Abbreviations: Bn, bornite; Ccp, chalcopyrite; Cv, covelline; Hem, hematite; Mt, magnetite; Po, pyrrhotite; Py, pyrite; and Qtz, quartz.

micro-drill bit ranged from 0.2 to 2 mm. A vacuum adsorption system was used to collect samples to ensure that the samples were pure. The specific parameters for this instrument and the sampling methods used in this study were described previously (Dong et al., 2013). Because of the interpenetration of the late-stage veins in the first-stage breccia, the micro-drill cannot completely avoid the late-stage minerals overlapping the early stage.

3.2. Pyrite trace element geochemistry

Standard thin sections were prepared for trace element analysis of pyrite. Trace element concentrations of pyrite from the stockwork and semi-massive sulfide-rich samples from the Suye hydrothermal field were analyzed using laser ablation inductively coupled plasma mass spectrometry (LA-ICP-MS) at the State Key Laboratory of Ore Deposit Geochemistry, Institute of Geochemistry, Chinese Academy of Sciences. A laser microprobe (ASI RESOLution-LR-S155) coupled with an excimer laser (Coherent Compex-Pro 193 nm ArF) was employed as a laser sampler with an ICP-MS instrument (Agilent 7700x) for the acquisition of ion-signal intensities. Argon gas was used as the transport gas, with a gas flow rate at 900 ml/min. Data were collected for 60 s after the signal intensity stabilized (generally after 30 s). The pit size, pulse frequency, and fluence were 26 μm, 5 Hz, and 3 J cm^2, respectively. Peru Py, an internal laboratory standard, was used to calibrate the contents of the S and Fe, GSE-1G and GSD-1G were used to calibrate the contents of the lithophile elements, and STDGL3 was used to calibrate the contents of the chalcophile and siderophile elements (Danyushevsky et al., 2011). A sulfide reference material (MASS-1) was analyzed to monitor the data quality during the MS measurements. The error in these test results was consistently within 20% of the accepted value.

3.3. Sulfur isotopes

Sulfur isotope ratios ($^{34}S/^{32}S$) were measured using a Thermo Finnigan MAT 253 isotope ratio mass spectrometer (Thermo Scientific, Bremen, Germany) at the State Key Laboratory of Ore Deposit Geochemistry, Institute of Geochemistry, Chinese Academy of Sciences, in Guiyang. The international measurement standard reference materials for the sulfur isotope measurement were IAEA-S-1 (Ag_2S reference material 8554; $\delta^{34}S_{V\text{-}CDT} = -0.3‰$), IAEA-S-2 (reference material 8555; $\delta^{34}S_{V\text{-}CDT} = 22.6‰$), and IAEA-S-3 (reference material 8529; $\delta^{34}S_{V\text{-}CDT} = -32.49‰$), which yielded a relative error (2σ) of $< 0.15‰$. All sulfur isotope ratios are reported in standard delta notation, where $\delta^{34}S = (R_{Sample}/R_{V\text{-}CDT} - 1) \times 1000$, and R is the $^{34}S/^{32}S$ of the sample of the Vienna Canyon Diablo Troilite reference.

3.4. Microthermometry

Microthermometry of fluid inclusions was conducted with a Linkam THMSG600IR Heating-freezing Stage at the Key Laboratory of Submarine Geosciences, Ministry of Natural Resources, China. The precision of the temperature measurements was approximately ±0.1 and ±2 °C for freezing and heating, respectively. The heating/freezing rate generally ranged from 0.2 °C/min to 5 °C/min but decreased to less than 0.2 °C/min near phase transformation. Salinities were calculated using the following equation (Bodnar and Vityk, 1994): Salinity (wt.%) $= -1.78(T_m) + 0.0442(T_m)^2 - 0.000557(T_m)^3$.

4. RESULTS

4.1. Mineral formation sequence

Based on mineral intergrowth and replacement textures, the mineralization process can be divided into stockwork and semi-massive stages, in which the stockwork stage could be further divided into an early disseminated pyrite-hematite stage, followed by a Cu–Fe sulfides + Fe oxides + quartz vein stage (Fig. 4).

(1) Disseminated mineralization stage (Substage I): The primary minerals formed in this stage are euhedral pyrite, hematite, and minor magnetite disseminated in the altered basalt. Pyrite crystals are generally less than 0.2 mm in diameter and intergrown with hematite (Fig. 3a, b) and magnetite, and are occasionally replaced by chalcopyrite (Fig. 3c). Pyrite abundance is approximately 5–10% by volume and generally exhibits residual structures (Fig. 3a).
(2) Cu-Fe sulfides + Fe-oxides + quartz stage (Substage II): The main minerals in the veins are quartz (40–50%), chalcopyrite (10–20%), pyrite (10–20%), magnetite (5–10%), hematite (5%), and minor bornite and pyrrhotite (<1%). The sulfide minerals occur as veins that are either disseminated or cross-cut the altered basalt rocks. Pyrite is mostly anhedral and often replaced by chalcopyrite (Fig. 3d). The magnetite precipitated in two generations: an early euhedral magnetite (Mt1), which is distributed in the quartz veins or intergrown with chalcopyrite (Fig. 3e), and a late-stage anhedral magnetite (Mt2), which occurs with hematite (Fig. 3e and 3f). Hematite is replaced by magnetite to form needle-like pseudomorphic crystals (Fig. 3f). Minor pyrrhotite also occurs as local replacement of chalcopyrite.
(3) Semi-massive stage (Substage III): The main minerals in this stage are quartz (70–80%), pyrite (10–15%), chalcopyrite (5–10%), bornite (3–5%), pyrrhotite (3–5%), and minor sphalerite (<1%). The pyrite is euhedral–anhedral (Fig. 3g-3i) and, occasionally, minor chalcopyrite, pyrrhotite, and sphalerite particles occur as inclusions (Fig. 3i). Chalcopyrite intergrown with bornite replaces pyrrhotite and pyrite in the quartz matrix (Fig. 3g). In this stage, minor basalt breccia also occurs. Minor quartz veins are present in this stage, and likely formed from the late-stage hydrothermal activity.

4.2. Pyrite trace element geochemistry

Pyrite from stockwork veins (substage I and II) has S and Fe concentrations that range from 53.46 to 57.11 wt.% (average ± SD = 53.68 ± 0.52 wt.%, N = 58), and 41.34 to 44.62 wt.% (44.43 ± 0.47 wt.%, N = 58), respectively. These concentrations are comparable to the pyrite from the semi-massive samples (substage III), which contain S and Fe concentrations that range from 53.46 to 54.50 wt.% (53.57 ± 0.17 wt.%, N = 52), and 43.49 to 44.71 wt.% (44.53 ± 0.18 wt.%, N = 52), respectively. The Au and Ag contents of pyrite from stockwork veins (substage I and II) are mostly below detection limit, and range from 0.1 to 0.9 ppm (0.2 ± 0.2 ppm, N = 18), and 0.6 to 13.1 ppm (2.6 ± 3.1 ppm, N = 24), respectively (Supplementary Table 1). Gold and Ag from substage III pyrite exhibit comparable but slightly higher values, ranging from 0.1 to 1.1 ppm (0.3 ± 0.2 ppm, N = 41), and 0.7 to 53.9 ppm (5.9 ± 8.4 ppm, N = 45), respectively. The concentration of As in pyrite from stockwork veins are slightly lower than that of substage III pyrite, with values of 0.4–58.9 ppm (9.5 ± 13.0 ppm, N = 56), and 0.4–89.0 ppm (15.8 ± 17.1 ppm, N = 51), respectively. However, pyrite from the stockwork samples exhibit significantly higher Co, and Ni contents (1541.8 ± 4455.1 ppm, N = 58; 254.1 ± 270.2 ppm, N = 58, respectively) than that of semi-massive samples (540.1 ± 789.5 ppm, N = 52; 1.8 ± 8.2 ppm, N = 48, respectively).

4.3. Sulfur isotopes

The sulfur isotopic composition of 39 micro-drill samples ranges from $\delta^{34}S_{V\text{-}CDT}$ = 4.4–11.3 ‰ (average ± SD = 9.01 ± 1.57 ‰; Table 1), and exhibits a nearly normal distribution, with a modal value between 9–10 ‰ (Fig. 5a). The stockwork (substages I and II), and semi-massive (substage III) sulfide minerals exhibit a trend of decreasing $\delta^{34}S$ values during the mineralization process (Fig. 5b). Overall, the sulfur isotope compositions

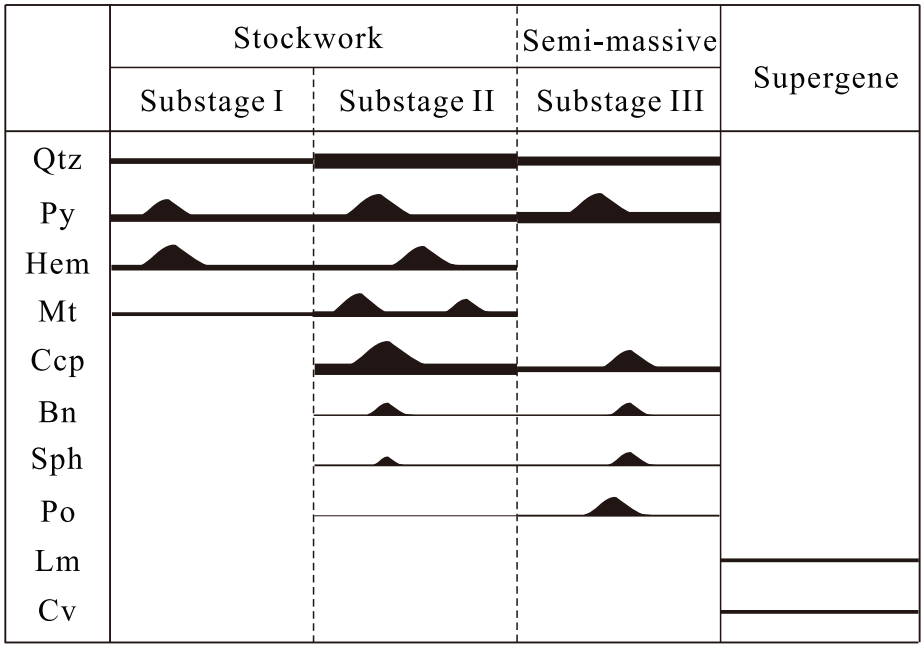

Fig. 4. Mineralization stages in the Suye hydrothermal field. Abbreviations: Lm, limonite; the others are the same as in Fig. 3. The width of the line indicates mineral abundance.

fall within the range of MORB ($\delta^{34}S_{V\text{-}CDT} = 0.1 \pm 0.5‰$; Sakai et al., 1984) and endmember seawater-derived sulfur (Fig. 6; $\delta^{34}S_{V\text{-}CDT}$ = 21.24‰; Tostevin et al., 2014).

4.4. Microthermometry

Liquid rich fluid inclusions were only observed in quartz veins from the stockwork and quartz matrix from semi-massive samples. The homogenization temperature and final ice melting temperature for the fluid forming the stockwork samples range from 279.2 to 347.6 °C (average ± SD = 313.8 ± 13.1 °C, N = 69, Table 2) and −8.0 to −3.2 °C (−5.6 ± 1.0 °C, N = 69), respectively. The calculated salinities range from 6.2 to 17.4 wt.% NaCl (11.5 ± 2.2 wt.% NaCl, N = 69). The semi-massive stage samples, however, exhibit a slightly lower homogenization temperature of 269.4–329.6 °C (294.6 ± 15.2 °C, N = 30; Fig. 7a) and salinity of 5.1–13.6 wt.% NaCl (10.0 ± 2.0 wt.% NaCl, N = 30; Fig. 7b). These observed salinities are significantly higher than that of seawater (3.4 wt.% NaCl).

5. DISCUSSION

5.1. Oxidizing mineral assemblages in the stockwork mineralization

Abundant Fe oxides were observed in the stockwork samples. The euhedral morphology of the hematite and magnetite crystals and their coexistence with chalcopyrite, quartz, and pyrite most likely indicate an authigenic origin. The occurrence of these Fe oxide minerals is different from occurrences at other vent fields, such as those on the Juan de Fuca, Turtle Pit, Broken Spur, Snake Pits, 15°51′ N and 15°05′ N MAR, Rainbow, Logatchev, and Ashadze, and 6°N EPR. In these fields, hematite and magnetite were commonly developed within Cu-Fe-rich chimneys or during seafloor mineralization due to shallow seawater infiltration (Fouquet et al., 2010; Dekov et al., 2018 and references therein), or formed during later diagenesis (e.g., in the Semenov vent fields; Melekestseva et al., 2014). On the other hand, oxidizing mineral assemblages formed by seawater interaction with both mafic and ultramafic basement rock were also observed on detachment faults along slow-spreading mid-ocean ridges, as well as in ophiolite sequences (Alt and Shanks, 1998; Kelley et al., 2001; Delacour et al., 2008), and supported by experimental results (Palandri and Reed, 2004). In serpentinized peridotites collected from the Lost City hydrothermal field, opaque minerals dominated by magnetite with relics of magmatic Al-spinels rimmed by ferritchromite were formed during oxidizing conditions at high water–rock ratios (Delacour et al., 2008). However, at Suye, hematite and magnetite were found to be major hydrothermal mineral phases (20–30% by volume) of the veins within the basaltic stockwork samples. Based on the mineral assemblages, the estimated oxygen fugacity of the fluids ($\log fO_2 > -27$; Fig. 8) for samples from the stockwork stages is higher than for most of the ultramafic, mafic and hybrid rock hosted hydrothermal fields (∼−33 to −28). Therefore, we conclude that the early stage ore-forming fluid responsible for the stockwork zone of the Suye hydrothermal system was under oxidizing conditions (Fig. 8). The semi-massive samples are characterized by high pyrite-chalcopyrite-pyrrhotite contents, suggesting that ore forming conditions became more reducing during the late stage mineralization.

Table 1
Sulfur isotope composition of the sulfide rich samples in Suye.

Stage	No	Substage	Sample	Serial No.	Description	$\delta^{34}S_{V\text{-}CDT}$(‰)	Main minerals
Stockwork	1	I	TVG05	6	basement rock	10.6	Py
	2	I	TVG05	7	basement rock	10.6	Py
	3	I	TVG21-2	1	basement rock Breccia	9.8	Py
	4	I	TVG21-2	6	basement rock Breccia	11.3	Py
	5	II	TVG21-6	8	Sulfide Breccia 1	9.0	Py
	6	II	TVG21-6	14	Sulfide Breccia 1	8.8	Py
	7	II	TVG21-6	18	Sulfide Breccia1	9.6	Py
	8	II	TVG21-2	3	Ccp + Py + Qtz vein	11.1	Ccp + Py
	9	II	TVG21-2	4	Ccp + Py + Qtz vein	10.9	Ccp + Py
	10	II	TVG21-2	5	Ccp + Py + Qtz vein	11.0	Ccp + Py
	11	II	TVG05	1	Py vein	8.1	Py
	12	II	TVG05	2	Py vein	10.3	Py
	13	II	TVG05	3	Py vein	9.4	Py
	14	II	TVG05	4	Py vein	10.4	Py
	15	II	TVG05	5	Hem + Py vein	8.7	Py
	16	II	TVG05	8	Hem + Py vein	8.9	Py
	17	II	TVG21-3	8	Sulfide Breccia 2	9.3	Py
	18	II	TVG21-6	6	Sulfide Breccia 2	10.3	Py
	19	II	TVG21-6	7	Sulfide Breccia 2	10.5	Py
	20	II	TVG21-6	9	Sulfide Breccia 2	9.2	Py
	21	II	TVG21-6	13	Sulfide Breccia 2	7.7	Py
	22	II	TVG21-6	16	Sulfide Breccia 2	9.6	Py
	23	II	TVG21-6	17	Sulfide Breccia 2	9.8	Py
	24	II	TVG21-6	1	Sulfide Breccia 2	10.6	Py
	25	II	TVG21-6	2	Sulfide Breccia 2	9.6	Py
Semi massive	26	III	TVG21-3	3	Py + Qtz Core	8.0	Py + Ccp + Po
	27	III	TVG21-3	4	Py + Qtz Core	9.1	Py + Ccp + Po
	28	III	TVG21-3	5	Py + Qtz Core	8.7	Py + Ccp + Po
	29	III	TVG21-3	6	Py + Qtz Core	9.2	Py + Ccp + Po
	30	III	TVG21-3	7	Py + Qtz Core	8.0	Py + Ccp + Po
	31	III	TVG21-6	3	Py + Qtz vein	7.0	Py
	32	III	TVG21-6	4	Py + Qtz vein	8.1	Py
	33	III	TVG21-6	5	Py + Qtz vein	7.8	Py
	34	III	TVG21-6	12	Py + Qtz vein	9.8	Py
	35	III	TVG21-6	15	Py + Qtz vein	7.4	Py
	36	III	TVG21-3	1	Qtz + Py crust	4.4	Py
	37	III	TVG21-3	2	Qtz + Py crust	6.9	Py
	38	III	TVG21-6	10	Qtz vein	5.1	Py
	39	III	TVG21-6	11	Qtz vein	6.9	Py

Note: The serial numbers represent the micro drilling samples, and their locations are shown in Fig. 2. Mineral abbreviations are the same as in Fig. 3.

5.2. The ultramafic reaction zone

Although we observed and collected only basaltic samples in the vicinity of Suye, there is evidence that indicates an ultramafic influence in the subseafloor mineralization. Trace element enrichment in sulfide minerals in seafloor hydrothermal systems are mainly controlled by the composition of their source rocks (Patten et al., 2016; Wohlgemuth-Ueberwasser et al., 2015), and depositional conditions (Keith et al., 2016; Grant et al., 2018). During alteration of peridotite, arsenic preferentially partitions into serpentinite, relative to other fluid-mobile elements (e.g., Au and Ag; Deschamps et al., 2013). The solubility and transport potential of Au in hydrothermal fluids would be enhanced by an increase in H_2S (Stefánsson and Seward, 2004), thus causing the resulting fluids and precipitates to be relatively depleted in As (Deschamps et al., 2013) and elevated Au/As and Ag/As ratios, compared to mafic to felsic rock hosted systems (Keith et al., 2016). In addition, ultramafic rocks generally contain significantly higher Ni and Co (>1500 ppm and >100 ppm, respectively, Dessimoulie et al., 2020) than mafic rocks (~100 ppm and 40–50 ppm, respectively; Yu and Dick, 2020), that likely contributed to the observed high concentrations of Ni and Co in stockwork mineralization from ultramafic related fields (Marques et al., 2007). Temperature and sulfur fugacity (fS_2) also play an important role in the incorporation of Co and Ni into pyrite. Cobalt preferentially enters the pyrite crystal lattice at high temperatures (Keith et al., 2016), whereas increasing sulfur fugacity causes increased Ni substitution and relatively lower Co/Ni ratios (Meng et al., 2020).

At Suye, results of in situ LA-ICP-MS analysis of pyrite from the stockwork samples show both high contents of Co

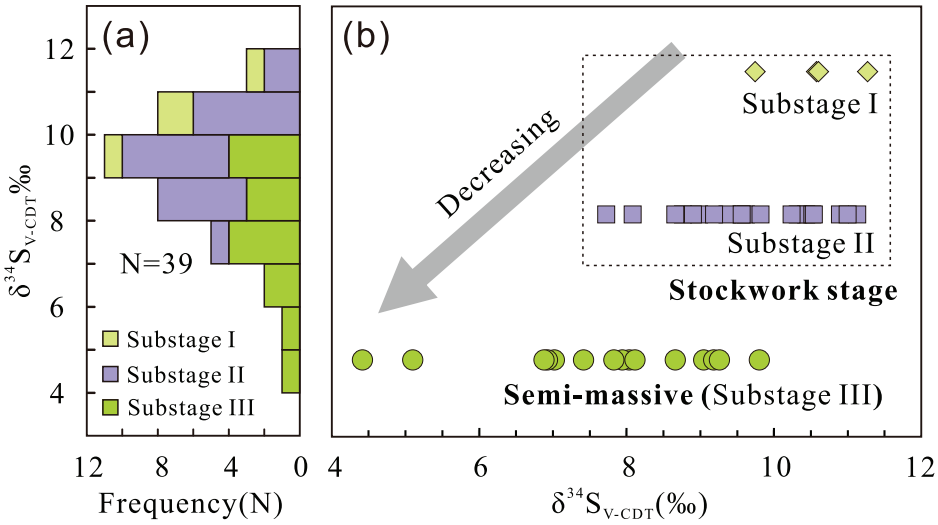

Fig. 5. (a) Histogram of sulfur isotope compositions for Suye; (b) Decreasing sulfur isotope compositions from stockwork to semi-massive stage.

and Ni, while the semi-massive pyrite exhibit high Co content and low Ni content (Fig. 9a; Supplementary Table 1). Because the studied stockwork and semi-massive samples were formed under relatively high temperature (average homogenization temperatures of 313.8 °C and 294.6 °C, respectively), and thus indicate relatively high sulfur fugacity (fS_2) of the substage I fluid, this observation is consistent with the occurrence of high oxidizing mineral assemblages. However, regardless of mineralization types, the studied pyrites all have low As and high Au/As, Ag/As and Ni/As ratios (Supplementary Table 1) that are comparable with those of stockwork, massive and sulfide chimneys from ultramafic hosted Tianzuo field, the hybrid Kairei, TAG and Longqi-1 fields, but different from those of the mafic hosted Meso zone and Wocan field, and fields at 1–2°S, and 5°S East Pacific Rise (Fig. 9b-9d). Because the different mineralization types represent a broad range of mineralizing conditions, these geochemical characteristics are most likely inherited from their source, which includes both mafic and ultramafic rocks. At Suye, deep tow observations indicate that the exposed wall rock along the detachment fault scarps are exclusively basalts, consistent with the magnetic low that was probably caused by alteration of mafic rocks revealed by recent near bottom magnetic survey (Wu et al., 2021). The velocity structure obtained by wide angle seismic observation suggest a mafic crustal thickness of 3–6 km in this area (isovelocity contour 7.0 km/s; Fig. 1c; Zhao et al., 2013; Tao et al., 2020). Thus, the ultramafic signals observed in trace elements in pyrite from the stockwork samples must reflect a relatively deep hydrothermal circulation through the basaltic layer into the ultramafic rocks. Pyrite from the semi-massive samples have comparable trace element contents with those of the hybrid Longqi-1, Kairei and TAG field (Fig. 9), but comparatively lower Ni contents than those of the stockwork samples, likely due to preferential deposition of Ni in stockwork mineralization under higher temperature (Marques et al., 2007).

5.3. High seawater flux involved in the mineralization process

The sulfur isotope data suggest that the oxidizing hydrothermal fluid in Suye was generated at very high water/rock ratio. In sediment-starved MOR hydrothermal systems, the sulfur is derived primarily from two sources: MORB-derived S ($\delta^{34}S_{V\text{-}CDT}$ = 0.1 ± 0.5‰; Sakai et al., 1984) and seawater sulfate ($\delta^{34}S_{V\text{-}CDT}$ = 21.2‰; Tostevin et al., 2014). In some cases, sulfur may also be derived from magmatic degassing and microbial related processes (Liao et al., 2018 and references therein). At Suye, the data show a range of $\delta^{34}S$ values that are greater than those of Longqi-1 (4.2–8.82 ‰, 7.19 ± 1.06‰, N = 40; Ye, 2012; Zeng et al., 2017), Duanqiao-1 (4.25–5.62 ‰, 4.67 ± 0.39 ‰, N = 29; Yang, 2017), and Yuhuang-1 (−1.38–8.73 ‰, 2.54 ± 2.65 ‰, N = 57; Liao et al., 2018) on the ultraslow-spreading SWIR (Liao et al., 2018), and most hydrothermal fields on other MOR systems, but close to the range at Rainbow (2.00–12.5 ‰, 7.73 ± 3.44 ‰, N = 39; Lein et al., 2001; Rouxel et al., 2004), TAG (0.35–10.27 ‰, 6.88 ± 1.08‰, N = 229; Chiba et al., 1998; Gemmell and Sharpe, 1998; Herzig et al., 1998; Knott et al., 1998) and Logatchev (4.50–9.60 ‰, 5.64 ± 1.65 ‰, N = 20; Rouxel et al., 2004) on the slow-spreading Mid Atlantic Ridge (Fig. 6), implying high contribution of seawater reduced sulfate. In addition, the stockwork (substages I and II), and semi-massive sulfide minerals exhibit a trend of decreasing $\delta^{34}S$ values during the mineralization process, with averages of 10.6 ± 0.6‰ (N = 4), 9.7 ± 0.9 ‰ (N = 21) and 7.6 ± 1.5 ‰ (N = 14) (Table 3), respectively. These results are generally consistent with observations of slightly increasing $\delta^{34}S$ values with depth in TAG, where the stockwork samples ($\delta^{34}S$ = 6–8‰) are enriched in the heavier sulfur isotope relative to the mound sulfide samples ($\delta^{34}S$ = 5–6‰; Petersen et al., 2000), but show higher values of about 2–4‰ in stockwork mineralization in Suye.

Studies have shown that isotope exchange between H_2S and SO_4^{2-} can take place in the subsurface prior to venting

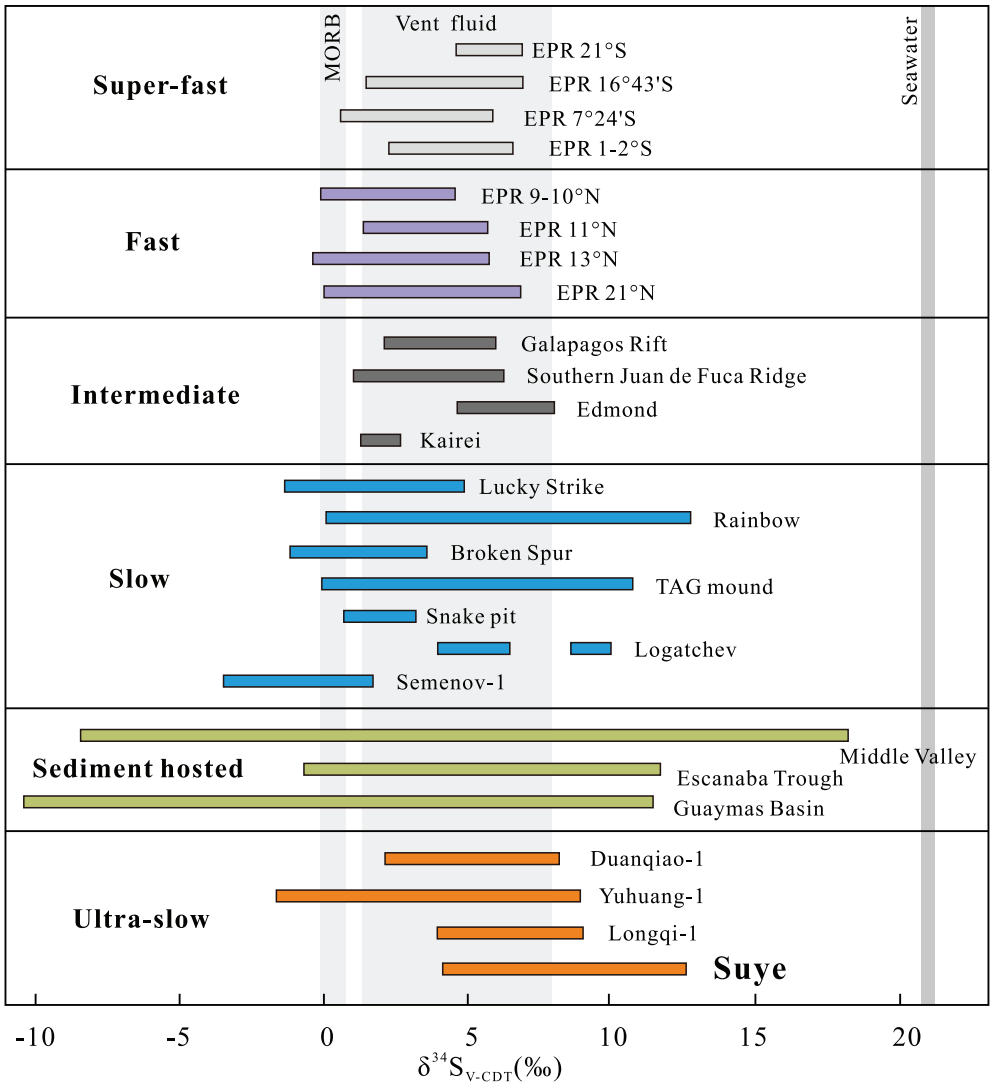

Fig. 6. Sulfur isotope comparison of Suye with other hydrothermal fields, modified after Liao et al. (2018). Data from Zeng et al. (2017) and references therein; Seawater (Tostevin et al., 2014); MORB (Sakai et al., 1984); Duanqiao-1 (Yang, 2017); Longqi-1 (Ye, 2012; Zeng et al., 2017); Yuhuang-1 (Liao et al., 2018); Suye (This study).

at the seafloor (Ohmoto et al., 1983; Ono et al., 2007). However, this exchange process generally results in relative minor fractionation (within ±1‰) compared to the variations of $\delta^{34}S$ values among sulfide minerals from different substages in Suye. Assuming that seawater-derived sulfate is quantitatively reduced to sulfide, and applying a two-component mixing model: $\delta^{34}S_{mix} = X \times \delta^{34}S_{seawater} + (1 - X) \times \delta^{34}S_{Basalt}$, the average amount of sulfur derived from reduced seawater sulfate ("X") in the mineralization process was calculated to gradually decrease from ~50% to ~45%, and further to ~36% for stockwork (substage I and II) and semi-massive sulfide samples (substage III), respectively (Table 3; Fig. 10a). These values, especially in the stockwork mineralization, are higher than average values of other hydrothermal fields on sediment-starved MOR systems (12–35%, Fig. 10b, Zeng et al., 2017 and references therein), indicating high seawater fluxes during sulfide formation in the stockwork zone of Suye. This conclusion is consistent with interpretations of deep-seated sulfate reduction into the oceanic crust at, for example, TAG (Petersen et al., 2000), ODP Hole 735B (Alford et al., 2011), and 15°20'N on the Mid-Atlantic Ridge (Alt et al., 2007). However, the higher $\delta^{34}S$ values at Suye, relative to these other sites, suggests a higher contribution of seawater-derived sulfur. The twin detachment fault in Suye may provide a high permeability substrate that allows influx of seawater sulfate into the system, causing relatively oxidizing conditions to form Fe-oxide minerals in stockwork zone.

5.4. Evolution of hydrothermal fluids

The timing and depth of oxidation of the hydrothermal fluids at Suye are key parameters for understanding the sub-seafloor evolution of the fluids. Firstly, the oxidizing conditions beneath Suye may be a result of a high degree of seawater infiltration along the first-stage matured

Table 2
Microthermometric data of Suye.

Stage	Host mineral	Fluid inclusion type	N	Size (μm)	Homogenization temperature(°C)	Final ice melting temperature(°C)	Salinity (wt.% NaCl)
Stockwork	Quartz	Liquid rich	69	4–15	279.2–347.6 (313.8 ± 13.1)	−8.0 to −3.2 (−5.6 ± 1.0)	6.2–17.4 (11.5 ± 2.2)
Semi massive	Quartz	Liquid rich	30	4–10	269.4–329.6 (294.6 ± 15.2)	−6.5 to −2.7 (−5.0 ± 0.9)	5.1–13.6 (10.0 ± 2.0)

Note: data in the brackets are average ± standard deviation.

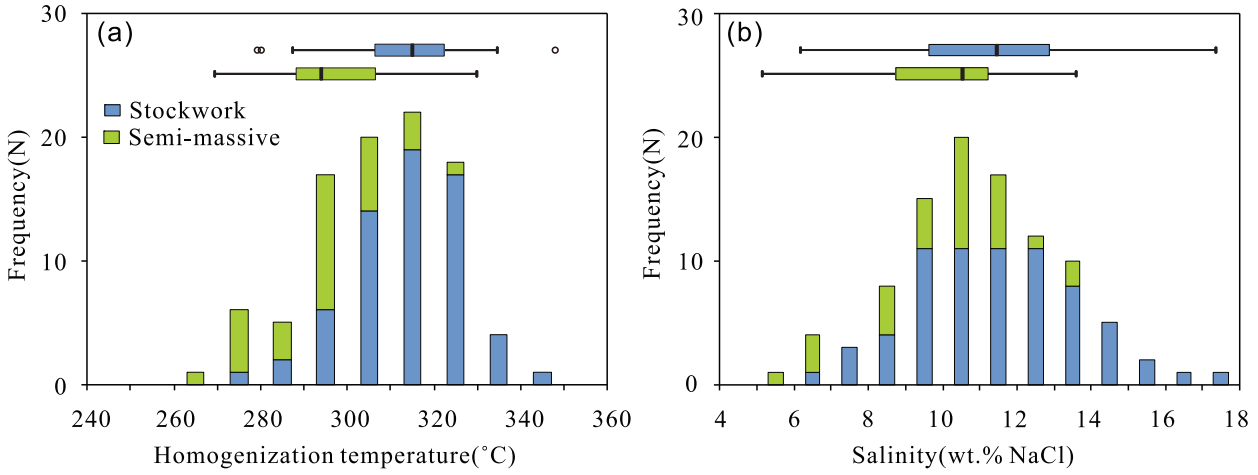

Fig. 7. Samples collected from Suye showing decreasing homogenization temperature and salinity from stockwork to semi-massive stages.

detachment fault (DF1) to the reaction zone, which creates high water/rock conditions. However, the adjacent active Longqi-1 hydrothermal field, located along the same detachment fault does not show characteristics of deep-rooted oxidized fluids (Tao et al., 2020), which make this explanation less plausible. In addition, it has been proposed

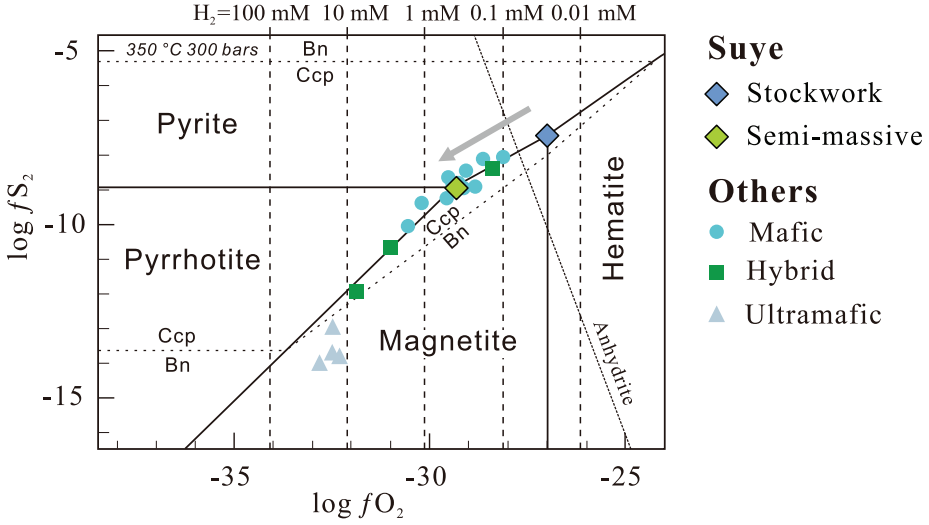

Fig. 8. Mineral assemblages showing stockwork samples of the Suye hydrothermal field formed under oxidizing condition than most of typical ultramafic-hosted, mafic-hosted and hybrid hydrothermal fields. The fO_2 and fS_2 conditions were determined by the mineral assemblages of pyrite-hematite-magnetite, and chalcopyrite-pyrite-pyrrhotite in the stockwork and semimassive mineralization, respectively. Stability fields for the Cu-Fe-S-O system and H_2 concentrations are from Kawasumi and Chiba (2017) and are calculated for 350 °C and 300 bar. Data base except for Suye were from Kawasumi and Chiba (2017).

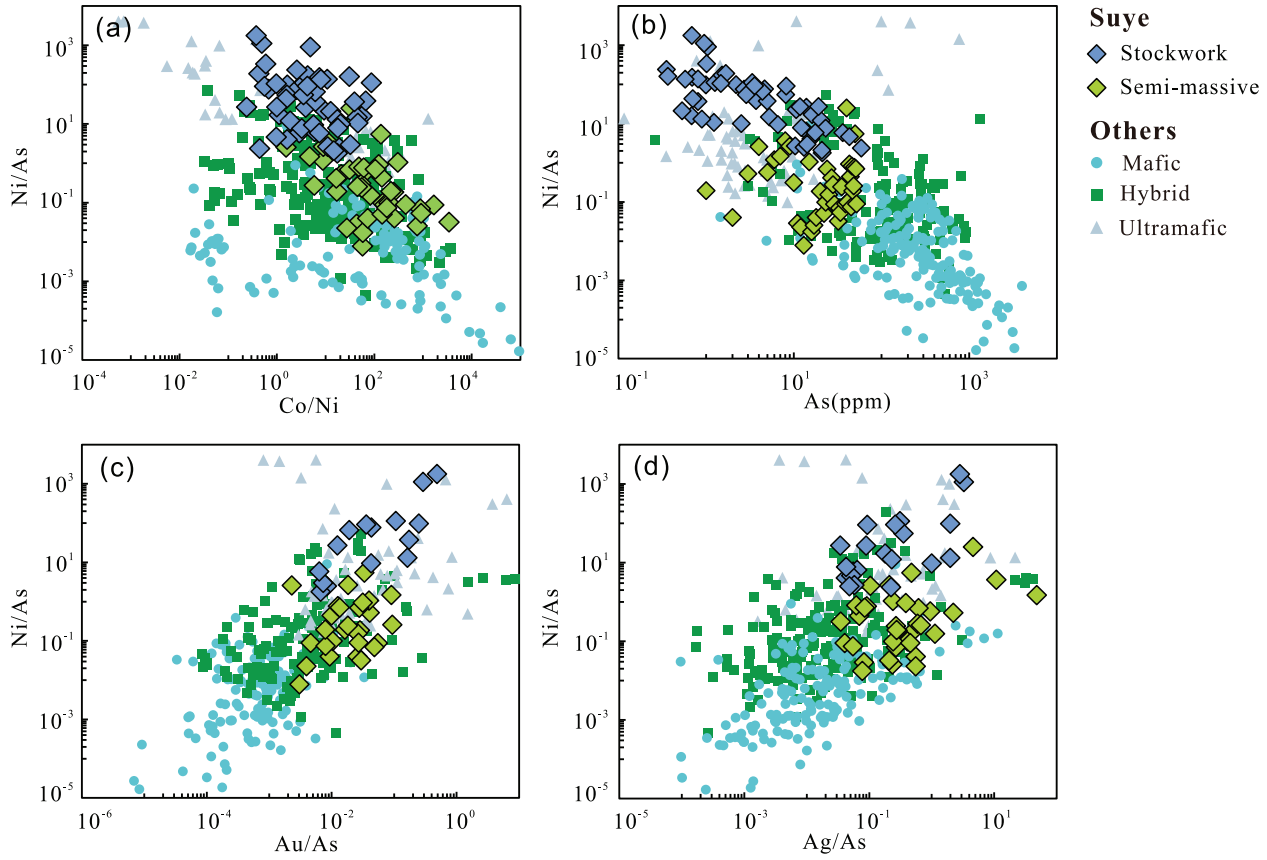

Fig. 9. (a) Variations in Co/Ni, (b) As, (c) Au/As, and (d) Ag/As vs. Ni/As in pyrite from hydrothermal systems at MOR systems. The Suye data are comparable to hybrid fields. Database: ultramafic-hosted: Logatchev, and Tianzuo (Keith et al., 2016; Ding et al., 2022); hybrid: TAG, Longqi-1, Kairei and Donglongjing-2 (Keith et al., 2016; Wang et al., 2018; Yuan et al., 2018; Grant et al., 2019; Liao et al., 2021); mafic-hosted: Meso zone, 5°S East Pacific Rise and Wocan (Keith et al., 2016; Wang et al., 2017), 1-2°S East Pacific Rise (Meng et al., 2020); and Tongguan (Wang et al., 2022).

that oxygen and sulfur fugacity in ultramafic systems will increase with water–rock interactions (i.e, serpentinization) over time. Serpentinization would stabilize relatively S-poor mineral phases such as pyrrhotite and heazlewoodite. With ongoing water–rock interactions, more S-rich mineral assemblages would form (Alt and Shanks, 1998; Schwarzenbach et al., 2014) due to the rock losing its reducing power with increasing serpentinizaiton (Frost, 1985; Klein and Bach, 2009), such as the observations in the Iberian Margin (Alt and Shanks, 1998), the southern wall of the Atlantis Massif (Delacour et al., 2008) and the Northern Apennines (Schwarzenbach et al., 2012). The final product of progressive water–rock reactions with increasing time-integrated fluid flux would produce a predicted assemblage of pyrite-magnetite-hematite. However, this process is unlikely to have occurred at Suye because: 1) complete serpentinization of ultramafic rocks under high temperature (200–300 °C) conditions would form abundant magnetite (Klein et al., 2014), but near bottom magnetic surveys revealed a magnetic low in Suye (Wu et al., 2021); and 2) the sulfide mineral assemblage of pyrite-chalcopyrite-sphalerite within chimneys in the adjacent active Longqi-1 field that formed along the same detachment fault indicate a more reduced environment (Tao et al., 2014), implying that the ultramafic basement has not been completely exhausted by serpentinization.

Alternatively, we propose that oxidizing conditions were caused by the mixing of infiltrated seawater with the ascending hydrothermal fluid. Microthermometry data indicate relatively high salinities of the fluid forming the stockwork (average ± SD = 11.5 ± 2.2 wt.% NaCl, N = 69) and semi-massive stage samples (average ± SD = 10.0 ± 2.0 wt.% NaCl, N = 30; Table 2). Previous studies revealed that hydration reactions may cause the increase of fluid salinity at low water/rock conditions in closed systems (Verlaguet et al., 2021), whereas, at Suye, the development of a deep detachment fault likely resulted in a more open system that facilitated the high seawater influx that is recorded by the high $\delta^{34}S$ values for the stockwork mineralization. In addition, a high salinity fluid may also be formed by mixture of the brine phase with its vapor phase produced by phase separation under low-pressure conditions (<25 Mpa; Coumou et al., 2009). However, the highest salinity observed in this study (17.4 wt.% NaCl; Table 2) is significantly higher than the max salinity produced by this mechanism (12 wt.% NaCl). Thus, the documented high salinities at Suye, compared with seawater (3.4 wt.% NaCl), must be the result of brine formation

Table 3
Calculation of sulfur isotopic composition of sulfides from the Suye hydrothermal field.

Stage	Substage	Minerals	$\delta^{34}S_{V\text{-}CDT}$(‰)					Reduced seawater sulfate (%)
			N	Min	Max	Average	Standard deviation	
Stockwork	I	Disseminated pyrite in altered basaltic debris	4	9.8	11.3	10.6	0.6	50 ± 3.0%
	II	Stockwork, Py + Ccp, cements the altered basaltic debris	21	7.7	11.1	9.7	0.9	45 ± 4.5%
Semi massive	III	Semi massive, Py + Po, cement early mineralization	14	4.4	9.8	7.6	1.5	36 ± 7.0%

due to phase separation lower in the system (Coumou et al., 2009; Verlaguet et al., 2021). Numerical modeling results demonstrating the process of phase separation and fluid flow under high pressure conditions (e.g., >35 MPa) produces a relatively steady high salinity upflow fluid (Coumou et al., 2009). The similar salinities of the stockwork and semi-massive samples is consistent with phase separation occurring deeper in the system. A deep brine source is also consistent with the inference that hydrothermal circulation in Suye likely percolates more than 3–6 km into the oceanic crust, as indicated by trace metal contents in pyrite that are indicative of reactions with ultramafic rocks that occur below the basalt cover. Numerical modelling suggests that the initial downflow of seawater from the recharge zone would be heated up to over 550 °C in the reaction zone to form the ascending hydrothermal fluid (Coumou et al., 2009; Tao et al., 2020). Components from serpentinization of ultramafic rocks under intermediate temperatures (200–400 °C; Mével, 2003) would be introduced to the fluid during fluid circulation. The phase separation process most likely occurred at a pressure of at least >55 MPa (i.e. 3 km below seafloor at water depth 2200–2400 m, and assuming hydrostatic pressure), because the fluid would be single phase between hydrostatic and lithostatic conditions during the infiltration into the oceanic crust (Fig. 11). When the fluids enter the detachment fault zone, the potential pressure decrease towards hydrostatic pressure leads to phase separation and formation of a high salinity brine and low salinity vapor phase (e.g., MAR 13°20′N, Verlaguet et al., 2021). The highest salinity of the brine phase would be around 60 wt.% NaCl, regardless of temperature (Bischoff and Pitzer, 1989) and 4–5 times volumetric dilution by seawater to produce the documented high salinity fluid.

During the mixing between high-temperature fluid and seawater in the subsurface, abiotic sulfate (SO_4^{2-}) reduction would significantly consume H_2 at temperatures above 150 °C, and increase the Eh values in the low-temperature diffuse fluid (McDermott et al., 2020). However, the homogenization temperature of fluid inclusions in the studied stockwork mineralization (peak value 300–320 °C, Fig. 7a) are comparable with the reported original high temperature fluid, ruling out the possibility of such mixing process. In addition, the fO_2 increase caused by gas loss is

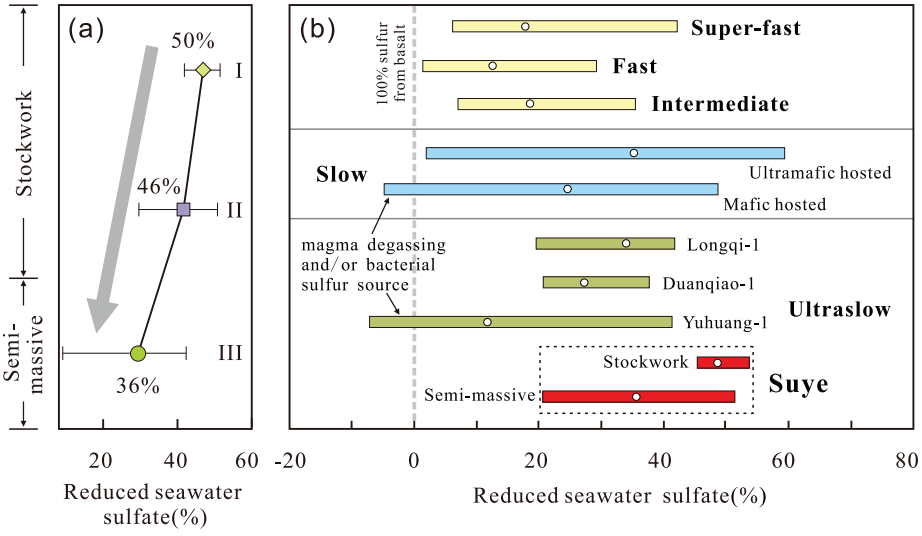

Fig. 10. (a) Decreasing seawater participation during the mineralization process from stockwork to semi-massive stage; (b) Comparison of seawater participation in the Suye formation with those of other fields on sediment-starved MOR systems. Ultramafic-hosted hydrothermal fields on slow spreading ridges show a wide range of reduced seawater sulfate content. However, the Suye field exhibit the highest average value (indicated by white circles). The reduced seawater sulfate content is calculated using formula: $\delta^{34}Smix = X \times \delta^{34}S_{seawater} + (1 - X) \times \delta^{34}S_{Basalt}$. Data from Zeng et al. (2017), Liao et al. (2018) and references therein, that the same as in Fig. 6.

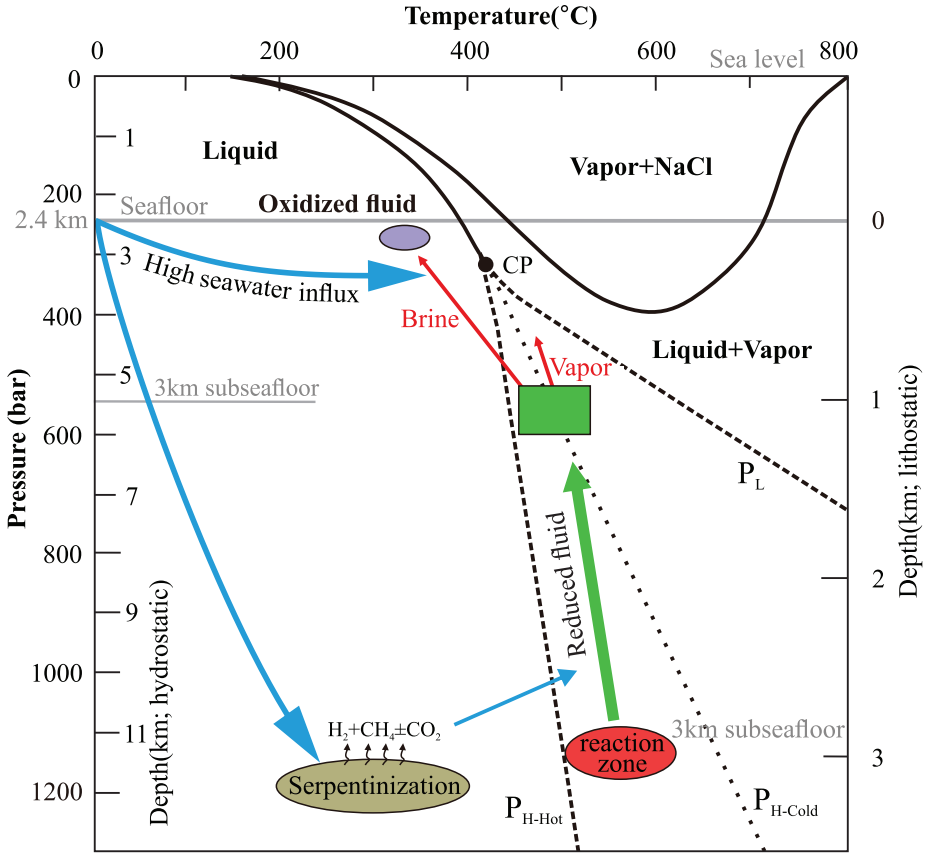

Fig. 11. Phase diagram showing the inferred fluid evolution process that occurs in Suye (phase diagram after Castelain et al., 2014). $P_{H\text{-}Cold}$, $P_{H\text{-}Hot}$ and P_L showing relationship between fluid pressure and depth for hydrostatic pressure under cold (100 bars/km) and hot (30 bars/km) gradients, and a lithostatic pressure gradient. Fluid infiltration in the oceanic crust occurs in single phase between lithostatic (P_L) and hydrostatic (P_H) and pressure. The original fluid from the reaction zone added H_2, CH_4 produced by serpentinization. Phase separation process most likely occurred during the transition from lithostatic to hydrostatic pressure when the fluid migrates to the detachment fault zone (assuming happed at least 3 km subseafloor). The ascending brine was diluted by high seawater influx to produce the observed oxidizing fluid. See text for details. CP: Critical point of seawater.

very small ($fO_2 < 1$) at such high temperature due to weak gas partitioning at near-critical conditions (Kawasumi and Chiba, 2017). Therefore, phase separation cannot cause such significant shift in fluid redox state. Alternatively, given 0.1–10 mM dissolved H_2 in fluids of typical hybrid hydrothermal fields (Fig. 8), the proposed 4–5 times seawater dilution is within the range required for shifting the fluid redox state to the observed oxidizing fluid (final dissolved $H_2 < 0.03$ mM, requiring 3–100 times dilution). It further implies that the oxidizing hydrothermal fluid was formed by seawater influx during ascent in the upflow zone. The high salinity fluid could further decrease the rate of serpentinization of olivine thus decreasing the H_2 flux into the system (Lamadrid et al., 2017). A large influx of oxidizing seawater into the upflow zone will shift the redox state of the ascending fluid enough to form the observed hematite-magnetite-pyrite assemblages. The reduction in fluid temperature associated with seawater mixing is consistent with the reduction in the homogenization temperatures of the stockwork mineralization (peak value 300–320 °C, Fig. 7a) compared with the maximum possible temperature (ca. 370 °C from the boiling curve of seawater; Bischoff and Pitzer, 1989), given a water depth of ~2200 m and the stockwork mineralization develops in the upper several hundred meters below seafloor. Continuing mineralization of the breccia would eventually reduce the permeability of the substrate, resulting in a decrease in the influx of local seawater and lower $\delta^{34}S$ values for the semi-massive stage sulfide mineralization.

5.5. Diverse fugacity of the detachment-fault-associated hydrothermal fluids

At the Dragon Horn oceanic core complex, Suye and the Longqi-1 field develop on the footwall and hanging wall of the DF2 of the twin detachment fault (Fig. 1b), respectively. Passive ocean bottom seismometer deployments and micro-earthquake studies suggest that the brittle/ductile boundary beneath this ridge segment is relatively uniform and that no focused melting occurs in this region (Zhao et al., 2013; Yu et al., 2018). Hydrothermal fluid circulation at Longqi-1, which is likely driven by a deep melt

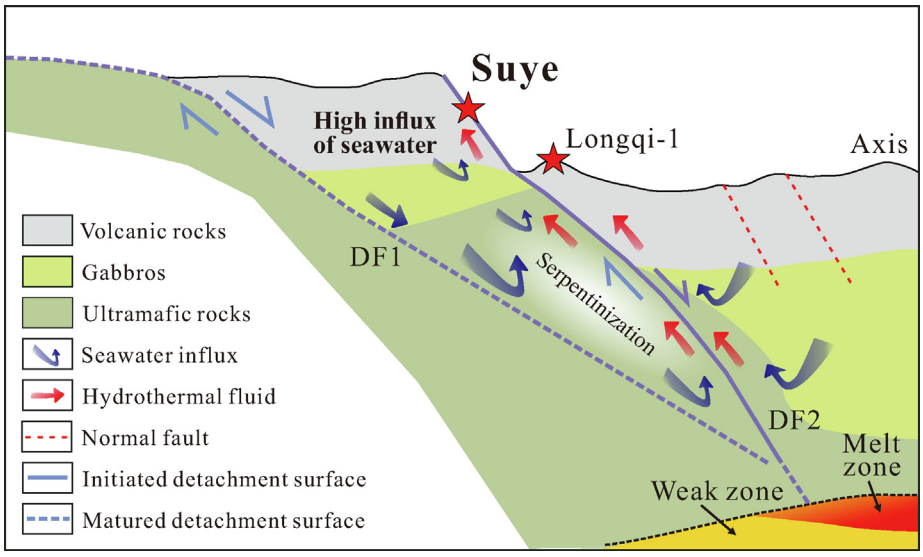

Fig. 12. Proposed hydrothermal fluid circulation at the Dragon Horn oceanic core complex (after Tao et al., 2020). Hydrothermal circulation at Longqi-1 was inferred to be approximately 6 km deeper than the Moho boundary (Tao et al., 2020). The oxidizing hydrothermal circulation in Suye likely resulted from its development between the twin detachment faults creating higher permeability than that of the Longqi-1 on the hanging wall close to the ridge axis. High seawater flux infiltration along the DF1 give rise to the high water/rock ratio in the subsurface and created the proposed oxidizing fluid. DF: Detachment fault. NF: Normal fault.

zone in the mantle, penetrates to approximately 6 km deeper than the Moho boundary (Tao et al., 2020), a depth that is considerably deeper than the inferred depths of circulation at TAG and Logachev-1 on the slow-spreading MAR (Demartin et al., 2007; Grevemeyer et al., 2013). Trace element concentrations in pyrite indicate the involvement of ultramafic rocks in Suye formation, also suggesting a relatively deep hydrothermal circulation. The formation of the Suye and Longqi-1 hydrothermal fields are both controlled by the secondary active detachment fault (DF2) on the Dragon Horn area (Fig. 1b). However, the Longqi-1 field is characterized by mineral assemblages of pyrite, chalcopyrite, and sphalerite (Tao et al., 2011). In contrast, the Suye hydrothermal field contains more oxidizing precipitates of Fe oxides associated with increased seawater penetration. This is probably due to the location of Suye which is between DF1 and DF2 of the twin detachment fault (Figs. 1b and 12), that creates a high permeability zone that facilitates increased seawater infiltration, relative to the Longqi-1field.

Other hydrothermal systems on mid-ocean ridges that contain abundant Fe-oxide minerals largely occur on an axial volcanic ridge (e.g., Turtle Pits, Broken Spur on the MAR, 9°46′N on East Pacific Rise, Butterfield et al., 1997; Haase et al., 2007), or on oceanic core complexes (e.g., Irina II in Logatchev, Dekov et al., 2018), and are interpreted to have formed due to shallow seawater infiltration into the seafloor. By contrast, our study suggests that the oxidizing fluid at Suye is formed deeper beneath the stockwork zone. Our results suggest that multistage detachment faults at ultraslow-spreading ridges can sustain both reducing and oxidizing hydrothermal fluids in the same fault system (Fig. 12), and thus focus higher seawater flux into the deep oceanic crust than current knowledge, therefore causing larger chemical and energy exchange between the ocean and crust on MOR systems.

6. CONCLUSION

Primary oxidized mineral assemblages were discovered from stockwork samples in the Suye hydrothermal field on the ultraslow spreading Southwest Indian Ridge. The low As, high Ni contents of pyrite from the stockwork samples suggest that the source of the metals in the hydrothermal fluids were of hybrid mafic–ultramafic origin associated with relatively deep hydrothermal circulation. The sulfur isotope compositions of the collected samples range from 4.4 to 11.3‰ with an average of 9.0‰. During the mineralizing process, the amount of seawater-derived sulfur in the hydrothermal system decreased from 50% at the stockwork to 36% at the semi-massive stage. These data, combined with results from fluid inclusion analyses, indicate that these samples formed by 4–5 times seawater dilution of a brine formed by phase separation of the original hydrothermal fluid associated with a multistage detachment fault and ultramafic rocks. On slow-ultraslow spreading ridges, such multistage detachment faults are widespread (Reston, 2018). Our results indicate that oxidized fluids may play a significant role in the mineralization processes at ultramafic-hosted hydrothermal systems. The sub-seafloor precipitation of high fO_2-fS_2 mineral assemblages has a significant impact on the composition and metal concentrations of the fluids that vent at the seafloor, and hence affects the composition of associated sulfide chimneys and mounds. Thus, our results call for a reevaluation of the fate of base metals in ultramafic hosted hydrothermal fields.

Declaration of Competing Interest

The authors declare that they have no known competing financial interests or personal relationships that could have appeared to influence the work reported in this paper.

ACKNOWLEDGMENT

This research was funded by the National Key Research and Development Program of China (2018YFC0309902), National Natural Science Foundation of China (42006074, 42127807, 42073010), Scientific Research Fund of the Second Institute of Oceanography, Ministry of Natural Resources (SZ2201), and China Ocean Mineral Resources R & D Association Project (DY135-S1-1-02). We would like to thank the captains and crews who contributed to the success of this project. We are also grateful for the constructive comments and suggestions from Prof. Esther Schwarzenbach, Prof. Jeffrey G. Catalano, Ph. D. Drew D. Syverson and another two anonymous reviewers.

APPENDIX A. SUPPLEMENTARY MATERIAL

Supplementary material to this article can be found online at https://doi.org/10.1016/j.gca.2022.04.025.

REFERENCES

Alford S. E., Alt J. C. and Shanks W. C. (2011) Sulfur geochemistry and microbial sulfate reduction during low-temperature alteration of uplifted lower oceanic crust: Insights from ODP Hole 735B. *Chem. Geol.* **286**, 185–195.

Alt J. C. and Shanks W. C. (1998) Sulfur in serpentinized oceanic peridotites: Serpentinization processes and microbial sulfate reduction. *J. Geophys. Res. [Atmos.]* **103**, 9917–9929.

Alt J. C., Iii W. C. S., Bach W., Paulick H., Garrido C. J. and Beaudoin G. (2007) Hydrothermal alteration and microbial sulfate reduction in peridotite and gabbro exposed by detachment faulting at the Mid-Atlantic Ridge, 15°20′N (ODP Leg 209): A sulfur and oxygen isotope study. *Geochem. Geophy. Geosy.* **8**, 13–23.

Bischoff J. L. and Pitzer K. S. (1989) Liquid-vapor relations for the system NaCl-H_2O: Summary of the P-T-X surface from 300°C to 500°C. *Am. J. Sci.* **289**, 217–248.

Bodnar R. J. and Vityk M. O. (1994) Interpretation of microthermaetric data for H_2O-NaCl fluid inclusions. In *Fluid Inclusions in Minerals: Methods and Applications* (eds. V. B. De and M. L. Frezzotti). Verginia Tech, Blaksberg, pp. 117–130.

Butterfield D. A., Jonasson I. R., Massoth G. J., Feely R. A., Roe K. K., Embley R. E., Holden J. F., Mcduff R. E., Lilley M. D. and Delaney J. R. (1997) Seafloor eruptions and evolution of hydrothermal fluid chemistry. *Philos. Trans. R. Soc. London Ser. A* **355**, 369–386.

Cannat M., Sauter D., Lavier L., Bickert M., Momoh E. and Leroy S. (2019) On spreading modes and magma supply at slow and ultraslow mid-ocean ridges. *Earth Planet. Sc. Lett.* **519**, 223–233.

Castelain T., Mccaig A. M. and Cliff R. A. (2014) Fluid evolution in an Oceanic Core Complex: A fluid inclusion study from IODP hole U1309 D-Atlantis Massif, 30°N, Mid-Atlantic Ridge. *Geochem. Geophy. Geosy.* **15**, 1193–1214.

Charlou J. L., Donval J. P., Fouquet Y., Jean-Baptiste P. and Holm N. (2002) Geochemistry of high H_2 and CH_4 vent fluids issuing from ultramafic rocks at the Rainbow hydrothermal field (36°14′ N, MAR). *Chem. Geol.* **191**, 345–359.

Chiba H., Uchiyama N. and Teagle D. A. H. (1998) Stable isotope study of anhydrite and sulfide minerals at the TAG hydrothermal mound, Mid-Atlantic Ridge, 26°N. *Proc. Ocean Drill. Program Sci. Res.* **158**, 85–90.

Connelly D. P., Copley J. T., Murton B. J., Stansfield K., Tyler P. A., German C. R., Van Dover C. L., Amon D., Furlong M. and Grindlay N. (2012) Hydrothermal vent fields and chemosynthetic biota on the world's deepest seafloor spreading centre. *Nat. Commun.* **3**, 620–628.

Coumou D., Driesner T., Weis P. and Heinrich C. A. (2009) Phase separation, brine formation, and salinity variation at Black Smoker hydrothermal systems. *J. Geophys. Res.* **114**, B3212.

Danyushevsky L., Robinson P., Gilbert S., Norman M., Large R., Mcgoldrick P. and Shelley M. (2011) Routine quantitative multi-element analysis of sulphide minerals by laser ablation ICP-MS: Standard development and consideration of matrix effects. *Geochem.: Explor. Environ. Anal.* **11**, 51–60.

Dekov V. M., Garbe-Schönberg D., Kamenov G. D., Guéguen B., Bayon G., Bindi L., Asael D. and Fouquet Y. (2018) Redox changes in a seafloor hydrothermal system recorded in hematite-chalcopyrite chimneys. *Chem. Geol.* **483**, 351–371.

Delacour A., Frueh-Green G. L., Bernasconi S. M. and Kelley D. S. (2008) Sulfur in peridotites and gabbros at Lost City (30° N, MAR): Implications for hydrothermal alteration and microbial activity during serpentinization. *Geochim. Cosmochim. Acta* **72**, 5090–5110.

Demartin B. J., Sohn R. A., Pablo C. J. and Humphris S. E. (2007) Kinematics and geometry of active detachment faulting beneath the Trans-Atlantic Geotraverse (TAG) hydrothermal field on the Mid-Atlantic Ridge. *Geology* **35**, 711–714.

Deschamps F., Godard M., Guillot S. and Hattori K. (2013) Geochemistry of subduction zone serpentinites: A review. *Lithos* **178**, 96–127.

Dessimoulie L., Delacour A., Guillaume D., Chevet J. and Cottin J. (2020) Major and trace elements exchanges during fluid-rock interaction at ultraslow-spreading oceanic lithosphere: Example of the South West Indian Ridge (SWIR). *Lithos* **352–353**, 105233.

Dick H. J., Lin J. and Schouten H. (2003) An ultraslow-spreading class of ocean ridge. *Nature* **426**, 405–412.

Ding T., Wang J., Tao C. H., Dias Á., Liang J., Wang Y., Chen J., Wu B. and Huang H. (2022) Trace-element compositions of sulfides from inactive Tianzuo hydrothermal field, Southwest Indian Ridge: Implications for ultramafic rocks hosting mineralization. *Ore Geol. Rev.* **140**, 104421.

Dong S. F., Chen D. Z., Qing H. R., Jiang M. S. and Zhou X. Q. (2013) In situ stable isotopic constraints on dolomitizing fluids for the hydrothermally-originated saddle dolomites at Keping, Tarim Basin. *Chin. Sci. Bull.* **58**, 2877–2882.

Elderfield H. and Schultz A. (1996) Mid-ocean ridge hydrothermal fluxes and the chemical composition of the ocean. *Annu. Rev. Earth Pl. Sc.* **24**, 191–224.

Fouquet Y., Cambon P., Etoubleau J., Charlou J. L., Ondréas H., Barriga F. J., Cherkashov G., Semkova T., Poroshina I., Bohn M., Donval J. P., Henry K., Murphy P. and Rouxel O. (2010) Geodiversity of hydrothermal processes along the Mid-Atlantic Ridge–Ultramafic-hosted mineralization: A new type of oceanic Cu-Zn-Co-Au volcanogenic massive sulfide deposit. In *Diversity of Hydrothermal Systems on Slow Spreading Ocean Ridges* (eds. P. A. Rona, C. W. Devey, J. Dyment and B. J. Murton). American Geophysical Union, Washington DC, pp. 321–367.

Frost B. R. (1985) On the stability of sulfides, oxides, and native metals in serpentinite. *J. Petrol.* **26**, 31–63.

Gemmell J. B. and Sharpe (1998) Detailed sulfur-isotope investigation of the TAG hydrothermal mound and stockwork zone, 26°N, Mid-Atlantic Ridge. *Proc. Ocean Drill. Program Sci. Res.* **158**, 71–84.

Grant H. L. J., Hannington M. D., Hardardóttir V., Fuchs S. H. and Schumann D. (2019) Trace metal distributions in sulfide scales of the seawater-dominated Reykjanes geothermal system: Constraints on sub-seafloor hydrothermal mineralizing processes and metal fluxes. *Ore Geol. Rev.* **116**, 103145.

Grant H. L. J., Hannington M. D., Petersen S., Frische M. and Fuchs S. H. (2018) Constraints on the behavior of trace elements in the actively-forming TAG deposit, Mid-Atlantic Ridge, based on LA-ICP-MS analyses of pyrite. *Chem. Geol.* **498**, 45–71.

Grevemeyer I., Reston T. J. and Moeller S. (2013) Microseismicity of the Mid-Atlantic Ridge at 7° S–8° 15′ S and at the Logatchev Massif oceanic core complex at 14° 40′ N–14° 50′ N. *Geochem. Geophys. Geosyst.* **14**, 3532–3554.

Haase K. M., Petersen S., Koschinsky A., Seifert R., Devey C. W., Keir R., Lackschewitz K. S., Melchert B., Perner M. and Schmale O. (2007) Young volcanism and related hydrothermal activity at 5°S on the slow-spreading Southern Mid-Atlantic Ridge. *Geochem. Geophys. Geosyst.* **8**, Q11002.

Hannington M. D., Galley A. G., Herzig P. M. and Petersen S. (1998) 28. Comparison of the TAG mound and stockwork complex with Cyprus-type massive sulfide deposits. *Proc. Ocean Drill. Program Sci. Res.* **158**, 389–415.

Hannington M. D., Jamieson J., Monecke T., Petersen S. and Beaulieu S. (2011) The abundance of seafloor massive sulfide deposits. *Geology* **39**, 1155–1158.

Herzig P. M., Petersen S. and Hannington M. D. (1998) Geochemistry and sulfur-isotopic composition of the TAG hydrothermal mound, Mid-Atlantic Ridge, 26 °N. *Proc. Ocean Drill. Program Sci. Res.* **158**, 47–70.

Jamieson J. W. and Gartman A. (2020) Defining active, inactive, and extinct seafloor massive sulfide deposits. *Marine Policy* **117**, 103926.

Kawasumi S. and Chiba H. (2017) Redox state of seafloor hydrothermal fluids and its effect on sulfide mineralization. *Chem. Geol.* **451**, 25–37.

Keith M., Haeckel F., Haase K. M., Schwarz-Schampera U. and Klemd R. (2016) Trace element systematics of pyrite from submarine hydrothermal vents. *Ore Geol. Rev.* **72**, 728–745.

Kelley D. S., Karson J. A., Blackman D. K., Frühgreen G. L., Butterfield D. A., Lilley M. D., Olson E. J., Schrenk M. O., Roe K. K. and Lebon G. T. (2001) An off-axis hydrothermal vent field near the Mid-Atlantic Ridge at 30°N. *Nature* **412**, 145.

Klein F., Bach W., Humphris S. E., Kahl W., Jöns N., Moskowitz B. and Berquó T. S. (2014) Magnetite in seafloor serpentinite—some like it hot. *Geology* **42**, 135–138.

Klein F. and Bach W. (2009) Fe-Ni-Co-O-S phase relations in peridotite–seawater interactions. *J. Petrol.* **50**, 37–59.

Knott R., Fouquet Y., Honnorez J., Petersen S., Bohn M. and Herzig P. M. (1998) Petrology of hydrothermal mineralization: A vertical section through the TAG mound. *Proc. Ocean Drill. Program Sci. Res.* **158**, 5–26.

Lamadrid H. M., Rimstidt J. D., Schwarzenbach E. M., Klein F., Ulrich S., Dolocan A. and Bodnar R. J. (2017) Effect of water activity on rates of serpentinization of olivine. *Nat. Commun.* **8**, 16107.

Lein A. Y., Cherkashev G. A., Ul'Yanov A. A., Ul'Yanova N. V., Stepanova T. V., Sagalevich A. M., Bogdanov Y. A., Gurvich E. G. and Torokhov M. P. (2001) Mineralogy and geochemistry of sulfide ores from the Logachev-2 and Rainbow fields: Similar and distinctive features. *Geochem. Int.* **41**, 271–294.

Liao S. L., Tao C. H., Li H. M., Barriga F. J. A. S., Liang J., Yang W. F., Yu J. Y. and Zhu C. W. (2018) Bulk geochemistry, sulfur isotope characteristics of the Yuhuang-1 hydrothermal field on the ultraslow-spreading Southwest Indian Ridge. *Ore Geol. Rev.* **96**, 13–27.

Liao S. L., Zhu C. W., Zhou J. P., Liu W. Y., Yv J. Y., Liang J., Yang W. F., Li W., Liu J. and Tao C. H. (2021) Distal axis sulfide mineralization on the ultraslow-spreading Southwest Indian Ridge: An LA-ICP-MS study of pyrite from the East Longjing-2 hydrothermal field. *Acta Oceanol. Sin.* **40**, 105–113.

Marques A. F. A., Barriga F. J. A. S. and Scott S. D. (2007) Sulfide mineralization in an ultramafic-rock hosted seafloor hydrothermal system: From serpentinization to the formation of Cu–Zn–(Co)-rich massive sulfides. *Mar. Geol.* **245**, 20–39.

Mccollom T. M. and Bach W. (2009) Thermodynamic constraints on hydrogen generation during serpentinization of ultramafic rocks. *Geochim. Cosmochim. Acta* **73**, 856–875.

Mcdermott J. M., Sylva S. P., Ono S., German C. R. and Seewald J. S. (2020) Abiotic redox reactions in hydrothermal mixing zones: Decreased energy availability for the subsurface biosphere. *PNAS* **117**, 20453.

Melekestseva I. Y., Tret'Yakov G. A., Nimis P., Yuminov A. M., Maslennikov V. V., Maslennikova S. P., Kotlyarov V. A., Beltenev V. E., Danyushevsky L. V. and Large R. (2014) Barite-rich massive sulfides from the Semenov-1 hydrothermal field (Mid-Atlantic Ridge, 13°30.87′ N): Evidence for phase separation and magmatic input. *Mar. Geol.* **349**, 37–54.

Meng X. W., Li X. H., Chu F. Y., Zhu J. H., Lei J. J., Li Z. G., Wang H., Chen L. and Zhu Z. M. (2020) Trace element and sulfur isotope compositions for pyrite across the mineralization zones of a sulfide chimney from the East Pacific Rise (1–2° S). *Ore Geol. Rev.* **116**, 103209.

Mével C. (2003) Serpentinization of abyssal peridotites at mid-ocean ridges. *C.R. Geosci.* **335**, 825–852.

Ohmoto H., Mizukami M., Drummond S. E., Eldridge C. S. and Lenagh T. C. (1983) Chemical processes of Kuroko formation. *Econ. Geol. Monogr.* **5**, 570–604.

Ono S., Iii W. C. S., Rouxel O. J. and Rumble D. (2007) S-33 constraints on the seawater sulfate contribution in modern seafloor hydrothermal vent sulfides. *Geochim. Cosmochim. Acta* **71**, 1170–1182.

Palandri J. L. and Reed M. H. (2004) Geochemical models of metasomatism in ultramafic systems: Serpentinization, rodingitization, and sea floor carbonate chimney precipitation. *Geochim. Cosmochim. Acta* **68**, 1115–1133.

Patten C. G. C., Pitcairn I. K., Teagle D. A. H. and Harris M. (2016) Sulphide mineral evolution and metal mobility during alteration of the oceanic crust: Insights from ODP Hole 1256D. *Geochim. Cosmochim. Acta* **193**, 132–159.

Petersen S., Herzig P. M. and Hannington M. D. (2000) Third dimension of a presently forming VMS deposit: TAG hydrothermal mound, Mid-Atlantic Ridge, 26 ° N. *Miner. Deposita* **35**, 233–259.

Reston T. (2018) Flipping detachments: The kinematics of ultra-slow spreading ridges. *Earth Planet. Sc. Lett.* **503**, 144–157.

Rouxel O., Fouquet Y. and Ludden J. N. (2004) Copper isotope systematics of the Lucky strike, Rainbow, and Logatchev Sea-Floor hydrothermal fields on the Mid-Atlantic ridge. *Econ. Geol.* **99**, 585–600.

Sakai H., Marais Des D. J., Ueda A. and Moore J. G. (1984) Concentrations and isotope ratios of carbon, nitrogen and sulfur in ocean-floor basalts. *Geochim. Cosmochim. Acta* **48**, 2433–2441.

Sarrazin J., Juniper S. K., Massoth G. and Legendre P. (1999) Physical and chemical factors influencing species distributions

on hydrothermal sulfide edifices of the Juan de Fuca Ridge, Northeast Pacific. *Mar. Ecol. Prog. Ser.* **190**, 89–112.

Schlindwein V. and Schmid F. (2016) Mid-ocean-ridge seismicity reveals extreme types of ocean lithosphere. *Nature* **535**, 276–279.

Schwarzenbach E. M., Frueh-Green G. L., Bernasconi S. M., Alt J. C., Shanks W. C. I., Gaggero L. and Crispini L. (2012) Sulfur geochemistry of peridotite-hosted hydrothermal systems: Comparing the Ligurian ophiolites with oceanic serpentinites. *Geochim. Cosmochim. Acta* **91**, 283–305.

Schwarzenbach E. M., Gazel E. and Caddick M. J. (2014) Hydrothermal processes in partially serpentinized peridotites from Costa Rica: Evidence from native copper and complex sulfide assemblages. *Contrib. Mineral. Petr.* **168**, 1079.

Seyfried, Jr, W. E. and Ding K. (1995) Phase equilibria in subseafloor hydrothermal systems: A review of the role of redox, temperature, pH and dissolved Cl on the chemistry of hot spring fluids at mid-ocean ridges. *Geophys Monogr.* **91**, 248–272.

Snook B., Drivenes K., Rollinson G. and Aasly K. (2018) Characterisation of mineralised material from the Loki's Castle hydrothermal vent on the Mohn's Ridge. *Minerals* **8**, 576.

Stefánsson A. and Seward T. M. (2004) Gold(I) complexing in aqueous sulphide solutions to 500°C at 500 bar. *Geochim. Cosmochim. Acta* **68**, 4121–4143.

Tao C. H., Jr W. E. S., Lowell R. P., Liu Y. L., Liang J., Guo Z. K., Ding K., Zhang H. T., Liu J., Qiu L., Egorov I., Liao S. L., Zhao M. H., Zhou J. P., Deng X. M., Li H. M., Wang H. C., Cai W., Zhang G. Y., Zhou H. W., Lin J. and Li W. (2020) Deep high-temperature hydrothermal circulation in a detachment faulting system on the ultra-slow spreading ridge. *Nat. Commun.* **11**, 1300.

Tao C. H., Li H. M., Huang W., Han X. Q., Wu G. H., Su X., Zhou N., Lin J., He Y. H. and Zhou J. P. (2011) Mineralogical and geochemical features of sulfide chimneys from the 49°39′ E hydrothermal field on the Southwest Indian Ridge and their geological inferences. *Chin. Sci. Bull.* **56**, 2828–2838.

Tao C. H., Li H. M., Jin X. B., Zhou J. P., Wu T., He Y. H., Deng X. M., Gu C. H., Zhang G. Y. and Liu W. O. (2014) Seafloor hydrothermal activity and polymetallic sulfide exploration on the Southwest Indian ridge. *Chin. Sci. Bull.* **59**, 2266–2276.

Tostevin R., Turchyn A. V., Farquhar J., Johnston D. T., Eldridge D. L., Bishop J. K. B. and Mcilvin M. (2014) Multiple sulfur isotope constraints on the modern sulfur cycle. *Earth Planet. Sc. Lett.* **396**, 14–21.

Verlaguet A., Bonnemains D., Mével C., Escartín J., Andreani M., Bourdelle F., Boiron M. C. and Chavagnac V. (2021) Fluid circulation along an oceanic detachment fault: Insights from fluid inclusions in silicified brecciated fault rocks (Mid-Atlantic Ridge at 13°20′N). *Geochem. Geophy. Geosy.* **22**, e2020G–e9235.

Wang S., Li C. S., Li B., Dang Y., Ye J., Zhu Z. W., Zhang L. C. and Shi X. F. (2022) Constraints on fluid evolution and growth processes of black smoker chimneys by pyrite geochemistry: A case study of the Tongguan hydrothermal field, South Mid-Atlantic Ridge. *Ore Geol. Rev.* **140**, 104410.

Wang Y. J., Han X. Q., Petersen S., Frische M., Qiu Z. Y., Cai Y. Y. and Zhou P. (2018) Trace metals distribution in sulfide minerals of the Ultramafic-Hosted hydrothermal systems: Example from the kairei vent field, Central Indian Ridge. *Minerals* **11**, 526.

Wang Y. J., Han X. Q., Petersen S., Frische M., Qiu Z. Y., Li H. M., Li H. L., Wu Z. C. and Cui R. Y. (2017) Mineralogy and trace element geochemistry of sulfide minerals from the Wocan Hydrothermal Field on the slow-spreading Carlsberg Ridge, Indian Ocean. *Ore Geol. Rev.* **84**, 1–19.

Webber A. P., Roberts S., Murton B. J. and Hodgkinson M. R. (2015) Geology, sulfide geochemistry and supercritical venting at the Beebe Hydrothermal Vent Field, Cayman Trough. *Geochem. Geophy. Geosy.* **16**, 2661–2678.

Wohlgemuth-Ueberwasser C. C., Viljoen F., Petersen S. and Vorster C. (2015) Distribution and solubility limits of trace elements in hydrothermal black smoker sulfides: An in-situ LA-ICP-MS study. *Geochim. Cosmochim. Acta* **159**, 16–41.

Wu T., Tivey M., Tao C., Zhang J., Zhou F. and Liu Y. (2021) An intermittent detachment faulting system with a large sulfide deposit revealed by multi-scale magnetic surveys. *Nat. Commun.* **12**, 5642.

Yang W. F. (2017) *Study of Hydrothermal Mineralization of Duanqiao Hydrothermal Field in Southwest Indian Ridge*. Zhejiang University, Ph. D. thesis (in Chinese with English abstract).

Yang W. F., Tao C. H., Li H. M., Liang J., Liao S. L., Long J. P., Ma Z. B. and Wang L. S. (2016) $^{230}Th/^{238}U$ dating of hydrothermal sulfides from Duanqiao hydrothermal field, Southwest Indian Ridge. *Mar. Geophys. Res.* **38**, 1–13.

Ye J. (2012) *Mineralization of Polymetallic Sulfides on Ultra-slow Spreading Southwest Indian Ridge at 49.6°E*. The Institute of Oceanology, Chinese Academy of Sciences, Ph. D. thesis (in Chinese with English abstract).

Yu X. and Dick H. J. B. (2020) Plate-driven micro-hotspots and the evolution of the Dragon Flag melting anomaly, Southwest Indian Ridge. *Earth Planet. Sc. Lett.* **531**, 116002.

Yu Z. T., Li J. B., Niu X. W., Rawlinson N., Ruan A. G., Wang W., Hu H., Wei X. D., Zhang J. and Liang Y. Y. (2018) Lithospheric structure and tectonic processes constrained by microearthquake activity at the central ultra-slow spreading Southwest Indian Ridge (49.2° to 50.8° E). *J. Geophys. Res. B: Solid Earth* **123**, 6247–6262.

Yuan B., Yu H. J., Yang Y. M., Zhao Y. X., Yang J. C., Xu Y., Lin Z. and Tang X. (2018) Zone refinement related to the mineralization process as evidenced by mineralogy and element geochemistry in a chimney fragment from the Southwest Indian Ridge at 49.6°E. *Chem. Geol.* **482**, 46–60.

Zeng Z. G., Ma Y., Chen S., Selby D., Wang X. Y. and Yin X. B. (2017) Sulfur and lead isotopic compositions of massive sulfides from deep-sea hydrothermal systems: Implications for ore genesis and fluid circulation. *Ore Geol. Rev.* **87**, 155–171.

Zhao M. H., Qiu X. L., Li J. B., Sauter D., Ruan A. G., Chen J., Cannat M., Singh S., Zhang J. Z. and Wu Z. L. (2013) Three-dimensional seismic structure of the Dragon Flag oceanic core complex at the ultraslow spreading Southwest Indian Ridge (49°39′ E). *Geochem. Geophy. Geosy.* **14**, 4544–4563.

Associate editor: Esther M. Schwarzenbach